The Astrophysical Journal, 973:151 (16pp), 2024 October 1 https://doi.org/10.3847/1538-4357/ad6567

FLIMFLAM DR1: The First Constraints on the Cosmic Baryon Distribution from Eight Fast Radio Burst Sight Lines

Ilya S. Khrykin[1,2], Metin Ata[3], Khee-Gan Lee[2,4], Sunil Simha[5], Yuxin Huang[2], J. Xavier Prochaska[2,5,6], Nicolas Tejos[1], Keith W. Bannister[7], Jeff Cooke[8,9], Cherie K. Day[10], Adam Deller[8], Marcin Glowacki[11], Alexa C. Gordon[12], Clancy W. James[11], Lachlan Marnoch[9,13,14,15], Ryan. M. Shannon[8], Jielai Zhang[8,16], and Lucas Bernales-Cortes[1]

[1] Instituto de Física, Pontificia Universidad Católica de Valparaíso, Casilla 4059, Valparaíso, Chile; i.khrykin@gmail.com
[2] Kavli IPMU (WPI), UTIAS, The University of Tokyo, Kashiwa, Chiba 277-8583, Japan
[3] The Oskar Klein Centre, Department of Physics, Stockholm University, AlbaNova University Centre, SE 106 91 Stockholm, Sweden
[4] Center for Data-Driven Discovery, Kavli IPMU (WPI), UTIAS, The University of Tokyo, Kashiwa, Chiba 277-8583, Japan
[5] University of California, Santa Cruz, 1156 High St., Santa Cruz, CA 95064, USA
[6] Division of Science, National Astronomical Observatory of Japan, 2-21-1 Osawa, Mitaka, Tokyo 181-8588, Japan
[7] ATNF, CSIRO, Space and Astronomy, PO Box 76, Epping, NSW 1710, Australia
[8] Centre for Astrophysics and Supercomputing, Swinburne University of Technology, Hawthorn, VIC 3122, Australia
[9] AR. Centre of Excellence for All Sky Astrophysics in 3 Dimensions (ASTRO 3D), Australia
[10] Department of Physics, McGill University, Montreal, QC H3A 2T8, Canada
[11] International Centre for Radio Astronomy Research (ICRAR), Curtin University, Bentley, WA 6102, Australia
[12] Center for Interdisciplinary Exploration and Research in Astrophysics (CIERA) and Department of Physics and Astronomy, Northwestern University, Evanston, IL 60208, USA
[13] School of Mathematical and Physical Sciences, Macquarie University, NSW 2109, Australia
[14] Astrophysics and Space Technologies Research Centre, Macquarie University, Sydney, NSW 2109, Australia
[15] Australia Telescope National Facility, CSIRO Space and Astronomy, P.O. Box 76, Epping, NSW 1710, Australia
[16] AR. Centre of Excellence for Gravitational Wave Discovery (OzGrav), Hawthorn, VIC 3122, Australia
Received 2024 January 31; revised 2024 July 4; accepted 2024 July 17; published 2024 September 27

Abstract

The dispersion measure of fast radio bursts (FRBs), arising from the interactions with free electrons along the propagation path, constitutes a unique probe of the cosmic baryon distribution. Their constraining power is further enhanced in combination with observations of the foreground large-scale structure and intervening galaxies. In this work, we present the first constraints on the partition of the cosmic baryons between the intergalactic medium (IGM) and circumgalactic medium (CGM), inferred from the FLIMFLAM spectroscopic survey. In its first data release, the FLIMFLAM survey targeted galaxies in the foreground of eight localized FRBs. Using Bayesian techniques, we reconstruct the underlying ∼Mpc-scale matter density field that is traced by the IGM gas. Simultaneously, deeper spectroscopy of intervening foreground galaxies (at impact parameters $b_\perp \lesssim r_{200}$) and the FRB host galaxies constrains the contribution from the CGM. Applying Bayesian parameter inference to our data and assuming a fiducial set of priors, we infer the IGM cosmic baryon fraction to be $f_{\rm igm} = 0.59^{+0.11}_{-0.10}$ and a CGM gas fraction of $f_{\rm gas} = 0.55^{+0.26}_{-0.29}$ for $10^{10}\,M_\odot \lesssim M_{\rm halo} \lesssim 10^{13}\,M_\odot$ halos. The mean FRB host dispersion measure (rest-frame) in our sample is $\langle {\rm DM_{host}} \rangle = 90^{+29}_{-19}$ pc cm^{-3}, of which $\langle {\rm DM^{unk}_{host}} \rangle = 69^{+28}_{-19}$ pc cm^{-3} arises from the host galaxy interstellar medium (ISM) and/or the FRB progenitor environment. While our current $f_{\rm igm}$ and $f_{\rm gas}$ uncertainties are too broad to constrain most galactic feedback models, this result marks the first measurement of the IGM and CGM baryon fractions, as well as the first systematic separation of the FRB host dispersion measure into two components: arising from the halo and from the inner ISM/FRB engine.

Unified Astronomy Thesaurus concepts: Missing mass (1068); Intergalactic gas (812); Circumgalactic medium (1879); Cosmic web (330); Redshift surveys (1378)

1. Introduction

As the gravitational pull of (primarily) dark matter forms the cosmic web, complex and nonlinear astrophysical processes conspire to redistribute the baryonic matter. This occurs especially in the potential wells of dark matter halos, where galaxies form and produce supernovae and active galactic nuclei (AGN). Stellar and AGN explosions and radiation heat the gas, pushing it outward. These "feedback" processes can entirely evacuate the potential wells of baryons, driving them far beyond the halo's virial radius (e.g., Sorini et al. 2022; Ayromlou et al. 2023; Khrykin et al. 2023).

In parallel, the collapse of matter onto the filamentary structures that comprise the cosmic web is predicted to shock-heat the gas and produce the warm-hot intergalactic medium (WHIM; Cen & Ostriker 1999) that may be the dominant phase of baryons in the $z \sim 0$ Universe (e.g., Nevalainen et al. 2015). This WHIM was introduced originally to "explain" the missing baryons problem highlighted by Fukugita et al. (1998): the nondetection of ∼40% of the mass density of baryons, ρ_b. Yet despite sustained attempts over the past 20+ yr (e.g., Lehner et al. 2007; Tripp et al. 2008; Narayanan et al. 2009; Prochaska et al. 2011; Tejos et al. 2016; Nicastro et al. 2018; de Graaff et al. 2019), observational evidence for the WHIM has been scarce. As such, the (presumed) dominant phase of baryons in the present-day Universe is largely unexplored.

Table 1
List of FRBs in FLIMFLAM DR1 as Used in This Work

FRB	R.A. (deg)	Decl. (deg)	Redshift	Wide-field Data	Narrow-field Data	DM_{FRB} (pc cm^{-3})	References
20211127A	199.8088	−18.8381	0.0469	6dF	AAT	234.83	A. Deller et al. (2024, in preparation)
20211212A	157.3507	+01.3605	0.0713	SDSS	AAT	206.00	A. Deller et al. (2024, in preparation)
20190608A	334.0199	−07.8982	0.1178	SDSS, 6dF	SDSS, KCWI, MUSE	339.50	Macquart et al. (2020)
20200430A	229.7066	+12.3761	0.1608	SDSS, AAT	LRIS, DEIMOS, MUSE	380.10	Heintz et al. (2020)
20191001A	323.3516	−54.7477	0.2340	AAT	AAT, MUSE, GMOS-S	506.92	Bhandari et al. (2020)
20190714A	183.9795	−13.0207	0.2365	AAT	LRIS, DEIMOS, MUSE	504.70	Heintz et al. (2020)
20180924B	326.1052	−40.9000	0.3212	AAT	AAT, MUSE	362.40	Bannister et al. (2019)
20200906A	053.4956	−14.0833	0.3688	AAT	LRIS, DEIMOS, MUSE	577.80	Bhandari et al. (2020)

Note. From left to right, the columns show the ID of a given FRB, R.A. and decl. in equatorial J2000 coordinates, spectroscopic redshift, survey or instrument used to acquire the wide- and narrow-field spectroscopic foreground distribution of galaxies, and the overall observed DM_{FRB}, as well as the references for these estimates.

Recently, astronomers have leveraged an unexpected phenomenon to resolve the missing baryons problem: fast radio bursts (FRBs; Lorimer et al. 2007; Petroff et al. 2022). Encoded in the signal of these brief pulses of bright radio emission is the dispersion measure (DM_{FRB}), the integrated electron density along the sight line weighted by the scale factor $a \equiv 1/(1+z)$. Unlike most other probes of the intergalactic medium (IGM), DM_{FRB} is sensitive to the free electron density with only very tiny dependencies on the gas temperature and metallicity, potentially allowing for straightforward interpretations of the observations. To the extent that the vast majority of extragalactic baryons have been ionized since the end of cosmic reionization ($z \lesssim 6$; Gunn & Peterson 1965), the free electrons probed by FRBs represent a promising probe of the cosmic baryons.

Analyzing the first handful of localized FRBs, Macquart et al. (2020) confirmed the expectation that DM_{FRB} increases with host redshift. The positive correlation is consistent with the cosmic baryon density, Ω_b, derived from early Universe observations (e.g., Cooke et al. 2018). While this work (and subsequent FRB observations) has *detected* the missing baryons, the scarcity of the data and large variance in the Macquart relation caused by the unknown cosmic structures traversed by the FRB makes it challenging to determine the relative location of this otherwise invisible matter (but see Baptista et al. 2023 for first attempts from FRBs alone).

Thus motivated, we initiated the Foreground Line-of-sight Ionization Measurement From Lightcone AAOmega Mapping (FLIMFLAM) survey (Lee et al. 2022) to cross-correlate the DM_{FRB} with foreground structures and galactic halos. The primary goal of the FLIMFLAM survey is to acquire spectroscopic redshifts of galaxies and that way map their distribution in the foregrounds of well-localized FRBs. In addition, using a Bayesian algorithm for matter density reconstructions (Ata et al. 2015, 2017, 2021) allows us to significantly account for the scatter in the observed DM_{FRB} arising from the variance of the large-scale structures. Lee et al. (2022) have illustrated how this technique reduces the impact of cosmic variance by a factor of $\simeq$2–3 and simultaneously constrains the IGM and circumgalactic medium (CGM) baryon fractions with far greater precision than feasible with localized FRBs alone (see also Simha et al. 2020). Such a measurement would also provide insights into the galaxy formation and evolution models. For example, Khrykin et al. (2023) showed that different galaxy or AGN feedback prescriptions can drastically change the relative distribution of baryons between the circumhalo media of galaxies[17] vis-à-vis the low-density IGM outside of halos.

In this work, utilizing the "FRB foreground mapping" technique, we compare the observed DM_{FRB} of the sample of eight FRBs that are part of the first FLIMFLAM data release to predictions of baryon distribution from theoretical models and obtain the first observational constraints on cosmic baryons residing in the diffuse IGM and CGM gas of virialized halos. We utilize the Bayesian Markov Chain Monte Carlo (MCMC) algorithm that takes into account both observational and modeling uncertainties, allowing one to measure the partition of cosmic baryons with high precision.

This paper is organized as follows. In Section 2, we discuss the FLIMFLAM observations and archival data that have been used in this work. We describe the density reconstruction algorithm and its results in Section 3. In Section 4, we present and describe each component of the model for the observed FRB DM. We summarize our statistical algorithm for inferring the model parameters gathering the distribution of cosmic baryons and present the results of the parameter inference from the MCMC in Section 5. We discuss our findings in Section 6 and conclude in Section 7.

Throughout this work, we assume a flat ΛCDM cosmology with dimensionless Hubble constant $h = 0.673$, $\Omega_m = 0.315$, $\Omega_b = 0.046$, $\sigma_8 = 0.8$, and $n_s = 0.96$, consistent with the latest Planck results (Planck Collaboration et al. 2020).

2. Data Sample

In this paper, we analyze spectroscopic data obtained in the fields surrounding a sample of eight localized FRBs as listed in Table 1. Generally, we selected FRBs that were (i) localized to a host galaxy with a high probabilistic association of transients to their hosts posterior probability ($P(O|x) > 0.95$; see Aggarwal et al. 2021), (ii) located in regions of the sky with relatively low dust extinction ($E_{B-V} \lesssim 0.06$), and (iii) not believed to have a very large ($\gg$100 pc cm^{-3}) host contribution to the FRB DM (e.g., Lee et al. 2023; Simha et al. 2023). Our FRBs are derived from the Commensal Real-time ASKAP Fast Transients (CRAFT) survey conducted on the Australian Square Kilometre Array Pathfinder (ASKAP) radio telescope. These

[17] Variously known as the CGM, intragroup medium, or ICM, depending on the halo mass.

were then followed up with optical facilities by both the CRAFT and the Fast and Fortunate for FRB Follow-up collaborations[18] in order to identify the host galaxies and their redshift. At the time of observation (2020–2022), these sight lines listed in Table 1 represented the majority of known localized FRBs that fulfilled the aforementioned criteria.

2.1. Wide-field Data

The analysis in this paper combines the observed DMs from each FRB with detailed spectroscopic observations of their foreground galaxies. We will publish a separate paper (Huang et al. 2024) to describe the data in detail in conjunction with our first data release (DR1), but here we provide a broad overview.

The overall spectroscopic follow-up effort is dubbed the FLIMFLAM survey, which acknowledges the fact that a large fraction of the spectroscopic observations were carried out using the 2dF-AAOmega multiobject fiber spectrograph on the 3.9 m Anglo-Australian Telescope (AAT). The AAOmega data represent the bulk of our "wide" survey, which represents the shallowest but foundational tier of our "wedding cake" observational strategy, covering thousands of foreground galaxies over $\sim$3 deg^2 for each FRB field. The 3D positions of these galaxies will act as tracers for our density reconstruction of the foreground cosmic web toward individual FRB sight lines.

To select targets for our AAOmega observations, we typically used publicly available imaging survey catalogs such as those from the Dark Energy Survey (Abbott et al. 2021), the Panoramic Survey Telescope and Rapid Response System (Chambers et al. 2016), and the Dark Energy Camera Legacy Surveys (Dey et al. 2019). In each field, we then defined a magnitude limit to select galaxies for spectroscopy based on the redshift of the FRB; for $z_{\rm FRB} \lesssim [0.15, 0.25, 0.4]$, our nominal selection thresholds are dereddened Kron magnitudes of $r \leqslant [19.2, 19.4, 19.8]$, respectively. We dereddened the magnitudes using the milky Way dust maps of Schlegel et al. (1998). However, we had some confusion between the magnitude definitions from several of the imaging surveys that were only discovered after the spectroscopy was carried out. Cross-comparison between overlapping regions of different imaging surveys was then used to settle on a consistent magnitude definition. Henceforth, we used Kron magnitudes across all our targets. This generally resulted in small modifications to the overall spectroscopic completeness and radial selection functions (RSFs). The one exception is that the effective depth of the FRB 20200430A spectroscopy turned out to be $r \leqslant 18.6$, i.e., significantly shallower than the nominal selection threshold of $r \leqslant 19.2$ for this field. Therefore, we recalculated each field's RSFs to account for shallower observations.

With AAT/2dF-AAOmega, we can observe $\sim$350 science targets simultaneously in a field of radius $\sim1^\circ$ (i.e., 3.1 deg^2), but there were typically several thousand targets within our magnitude threshold within each 2dF pointing. We therefore designed 5–10 separate fiber plate configurations per field to obtain between 1200 and 2500 successful galaxy redshifts around each FRB position. The typical exposure times per galaxy range from 40 to 60 minutes depending on observing conditions, magnitude threshold, and dust extinction.

For our lowest-redshift sight lines (FRBs 20211127A, 20211212A, 20190608A, and 20200430A), we also included publicly available spectroscopic redshift survey data from the 6dF Galaxy Survey (Jones et al. 2009) and the New York University Value-Added Galaxy Catalog (Blanton et al. 2005) derived from the legacy Sloan Digital Sky Survey (SDSS; Abazajian et al. 2009). From these catalogs, we incorporated galaxies within 10° from the FRB position into our density reconstructions. The large footprint available from these wide-field surveys allowed us to cover a larger transverse distance than possible with the AAT observations. This allows a more accurate density reconstruction at the low-redshift end, which dominates the path length toward these FRBs.

2.2. Narrow-field Data

For galaxies that might be directly intersected by the FRB sight lines, it was our desire to reach fainter magnitudes than the $L \sim L^\star$ galaxies targeted as large-scale structure tracers in the wide-field data. Early on in FLIMFLAM, we decided to target fainter galaxies down to $r \leqslant 21.5$ within a $2\farcm5$ radius around each FRB, which we dubbed our "narrow-field" sample of galaxies. To obtain better signal-to-noise on these fainter galaxies, the "narrow-field" galaxies were each assigned fibers across two to three plate configurations within the same field to boost their total exposure time.

As our survey collaboration took shape, we obtained supplementary observing time on larger telescopes to target even fainter galaxies around our FRB sight lines. These include the DEIMOS and LRIS spectrographs at the W. M. Keck Observatory, GMOS on Gemini-South, and MUSE on UT4 of the Very Large Telescope (VLT). Multiobject slit masks were used with the Keck and Gemini spectrographs to target multiple galaxies within $\lesssim 10'$ of each FRB, corresponding to one to two virial radii of typical galaxy halo masses. The typical depth of these observations was $r \leqslant 22.5$, which corresponds to $L \sim 0.1\,L^\star$ for galaxies at $z \sim 0.3$ (see Figure 4 in Heintz et al. 2020).

In the case of our two lowest-redshift FRBs (20211127A and 20211212A), our nominal goal to observe $L \sim 0.1\,L^\star$ galaxies corresponds to a comparatively bright magnitude limit of $r \approx 20$, for which the 3.9 m AAT was deemed sufficient. We therefore observed two plates filled only with "narrow-field" galaxies over each of these two fields—the public SDSS and/or 6dF survey data were deemed sufficient for the "wide-field" large-scale structure tracer galaxies for these low-redshift FRB fields.

For all sight lines except FRB 20211127I and FRB 20211212A, we also managed to obtain integral field unit spectroscopy within $\sim 0\farcm5-1'$ around the FRB positions using the Keck II/KCWI and VLT/MUSE instruments, respectively. MUSE observations were conducted in its "wide-field adaptive optics" mode, i.e., covering a 1×1 arcmin^2 field, and each field was integrated for 4800 s corresponding to a 5σ depth of $r \sim 25$. The reduced and flux-calibrated cubes were summed in the spectral direction to produce a white-light image to identify sources. Spectra were extracted at the location of the identified sources. To produce the synthetic photometry for sources without data in existing public surveys, we used the g, r, i SDSS filter transmission curves but manually set transmission to 0 beyond the wavelength coverage of MUSE (4800–9300 Å). Furthermore, we set the transmission to 0 between 5800 and 5960 Å to account for the blocking filter used to avoid the light from the laser guide stars.

Finally, for each FRB field, we also queried the publicly available NASA/IPAC Extragalactic Database Local Volume Sample (Cook et al. 2023b), which contains spectroscopic and photometric information (from the Galaxy Evolution Explorer,

[18] https://sites.google.com/ucolick.org/f-4

Table 2
Parameters of the ARGO Reconstruction Volume for the FRB Fields Analyzed in This Work (See Table 1)

FRB	$d_{\rm FRB}$ (h^{-1} Mpc)	ARGO Volume Parameters		WF Survey Source	Limiting r mag	No. of Galaxies
		$N_x/N_y/N_z$	X; Y/Z Ranges (h^{-1} Mpc)			
20211127I	136.4	100/100/100	50–237.5; −93.75 to 93.75	6dF	15.60	1901
20211212A	210.1	100/100/100	50–237.5; −93.75 to 93.75	SDSS	17.77	15,321
20190608B	343.1	175/100/100	50–378.1; −93.75 to 93.75	SDSS	17.77	6640
				6dF	15.60	1273
20200430A	463.9	250/100/100	50–518.8; −93.75 to 93.75	SDSS	17.77	30,579
				AAT	18.60	260
20191001A	661.5	350/100/100	50–706.3; −93.75 to 93.75	AAT	19.40	1712
20190714A	677.4	350/100/100	50–706.3; −93.75 to 93.75	AAT	19.40	1270
20180924B	884.2	475/100/100	50–940.6; −93.75 to 93.75	AAT	19.80	2128
20200906A	1006.1	525/100/100	50–1034.4; −93.75 to 93.75	AAT	19.80	2186

Note. From left to right, the columns show the ID of a given FRB; the comoving distance to the FRB redshift, estimated with Equation (1); the number of reconstruction cells and the corresponding ranges along the X-, Y-, and Z-directions; the survey or instrument used to acquire wide-field spectroscopic data; the limiting r-band photometric magnitude used to select galaxies and estimate ASF/RSF; and the final number of galaxies used in ARGO reconstructions.

Two Micron All Sky Survey (2MASS), and AllWISE all-sky survey) about nearby galaxies at cosmic distances up to 100 cMpc that might intersect within impact parameters of $b_\perp \leqslant 2$ cMpc. This helps to supplement our foreground sample with relatively nearby galaxies that might intersect our FRB sight lines despite being outside the field of view of our dedicated observations.

3. Density Reconstructions

To obtain the underlying density field along the line of sight of each individual FRB, we utilize the ARGO numerical algorithm (Ata et al. 2015, 2017), based on works by Kitaura & Enßlin (2008), Jasche & Kitaura (2010), and Kitaura et al. (2010). In what follows, we outline the main properties of the ARGO reconstructions used in this work and refer the reader to more detailed descriptions given in the aforementioned manuscripts, as well as in Lee et al. (2022), where the multitracer extension is described.

3.1. ARGO Setup

ARGO is a fully Bayesian inference algorithm that applies a hybrid Monte Carlo (HMC) technique (Duane et al. 1987; Neal 2011) to reconstruct the evolved cosmic matter density fields given the observed redshift space distribution of galaxies on the light cone. The code depends only on the assumed cosmological and structure formation models, once the galaxy survey's selection functions and galaxy bias are taken into account. In addition, our version of ARGO adopts a prescription from Ata et al. (2021) that allows combining information from multiple individual spectroscopic surveys.

Before running ARGO, first, for a given FRB field, we set up a rectangular comoving reconstruction volume with cell sizes of 1.875 h^{-1} Mpc, where the X-axis is aligned with the line-of-sight direction to the FRB. Each volume contains $N_{\rm y} = N_{\rm z} = 100$ cells along the Y- and Z-axes, respectively, which represent the dimensions perpendicular to the line of sight. Our fields are narrow enough that we can adopt the flat-sky approximation and assume that the plane of the sky is always perpendicular to the line of sight. The number of cells along the X-axis is adjusted depending on the comoving distance between the observer and an FRB, given by

$$d_{\rm com} = \frac{c}{H_0}\int_0^{z_{\rm spec}} \frac{dz}{\sqrt{\Omega_{\rm M}(1+z)^3 + \Omega_\lambda}}. \quad (1)$$

Similar to Lee et al. (2022), we exclude the first 50 h^{-1} Mpc along the X-axis direction due to decreased ARGO performance at nearby comoving distances, where the light-cone distribution of galaxies becomes very narrow and the reconstructions would be noisy. For the first 50 h^{-1} Mpc of the path, we simply apply the mean cosmic $\langle {\rm DM_{igm}} \rangle$ value. In addition, we extend the X-axis beyond the line-of-sight position of a given FRB to avoid any potential boundary effects in the reconstructions near the FRB location. We provide a summary of the ARGO reconstruction volume properties in Table 2.

To simplify the $\rm DM_{igm}$ estimation at later stages of our analysis, the center of the coordinate system of the ARGO volume is chosen in such a way that an FRB is located at Cartesian coordinates $\boldsymbol{p} = \{X_{\rm frb}, Y = 0, Z = 0\}$. In order to place an FRB at these coordinates, we need to adopt a transformation between the on-sky and the corresponding Cartesian coordinates, provided by

$$\begin{aligned} X &= d_{\rm com}\cos\alpha\cos\delta, \\ Y &= d_{\rm com}\sin\alpha\cos\delta, \\ Z &= d_{\rm com}\sin\delta, \end{aligned}$$

where α and δ are the R.A. and decl. coordinates of the FRB and $d_{\rm com}$ is given by Equation (1). However, the resulting FRB coordinate vector is not yet aligned with the aforementioned coordinate system of the ARGO volume. Thus, we further estimate the rotation matrix that is then used to rotate the observed FRB frame to the correct ARGO coordinate system.

3.2. Galaxy Sample

As mentioned in Section 2.1, we adopt the wide-field sample of galaxies as tracers of the underlying matter density field in our ARGO density reconstructions. Therefore, the positions of the galaxies in these "wide-field" samples have to be mapped onto the ARGO coordinate system as well. Similar to the discussion in the previous section, we first convert galaxy on-sky coordinates to a Cartesian representation. Then, we adopt the rotation matrix found for the vector of FRB coordinates and

rotate these Cartesian coordinates to match the chosen ARGO coordinate system.

In addition to the coordinates of the galaxies, we supply ARGO with their respective stellar masses M_*. We estimate M_* with the publicly available CIGALE algorithm (Boquien et al. 2019), which fits a spectral energy distribution (SED) to the photometric information in multiple bands (see discussion in Section 2). For the SDSS and 6dF data, we query public archives to acquire the photometric magnitudes of the galaxies in our FRB fields. SDSS data have their own photometry, while for galaxies in the 6dF survey, we used magnitudes from 2MASS (Skrutskie et al. 2006) and the SuperCOSMOS survey that were used for target selection in the 6dF survey design (Jones et al. 2009).

Similar to Simha et al. (2023), we initialized the CIGALE algorithm assuming a delayed-exponential star formation history with no burst population, a synthetic stellar population described in Bruzual & Charlot (2003), the Chabrier (2003) initial mass function (IMF), dust attenuation models from Calzetti (2001), and a dust emission template from Dale et al. (2014), assuming an AGN fraction of $<20\%$.

CIGALE estimates the mean stellar masses with the corresponding uncertainties. In what follows, we adopt the mean stellar mass estimates from CIGALE. We also summarize the main properties of the wide-field samples that are used in the ARGO reconstructions in Table 2.

3.3. Groups and Clusters of Galaxies

Lee et al. (2023) illustrated the importance of taking into account foreground groups and clusters of galaxies when analyzing FRB DMs (see also Simha et al. 2023). Omitting this critical information might lead to erroneous conclusions about the nature of the observed DM. Likewise, such large cosmic structures might significantly affect the density reconstructions that do not capture such massive, nonlinear structures. Therefore, following the discussion in Lee et al. (2023), we apply an anisotropic friends-of-friends (FoF) group-finding algorithm (Tago et al. 2008; see also Tempel et al. 2012, 2014) on the galaxy samples in each FRB field.

This FoF finder adopts a redshift-dependent transverse linking length, $d_{\mathrm{LL},\perp}$, given by

$$d_{\mathrm{LL},\perp}(z) = d_{\mathrm{LL},0}[1 + a\ \arctan(z/z_*)], \tag{2}$$

where $d_{\mathrm{LL},0}$ is the linking length at a fiducial redshift and parameters a and z_* govern the redshift evolution. Such redshift-dependent modification of the linking length allows one to account for the decreasing completeness of the flux-limited spectroscopic surveys. The radial linking length, $d_{\mathrm{LL},\parallel}$, is then assumed to be simply proportional to $d_{\mathrm{LL},\perp}$. In this work, we adopt the following parameter values: $d_{\mathrm{LL},\perp} = 0.35\,h^{-1}$ Mpc, $a = 0.75$, $z_* = 0.1$, and $d_{\mathrm{LL},\parallel}/d_{\mathrm{LL},\perp} = 10$.

In order to have a more robust sample, we further refine the FoF algorithm findings by taking into account only the groups with richness parameter $N_{\mathrm{gal}} > 5$. Once the galaxy groups are identified in each FRB field, we remove their individual member galaxies from the compiled "wide-field" galaxy samples and replace them with the information (redshift, coordinates, and halo mass) on their corresponding group. The right-hand column of Table 2 shows the final numbers of halos that are derived from the "wide-field" sample of galaxies, serving as input to ARGO.

3.4. Selection Functions

The final ingredient of the ARGO machinery is the information about the angular selection functions (ASFs) and RSFs of the various wide-field surveys, listed in Table 1. It is crucial to incorporate this information to accurately determine, e.g., whether a given underdensity of galaxies within the survey volume is due to a cosmic void or a lack of observations within that region. In this section, we briefly outline the basic aspects of the ASF/RSF calculations and refer the interested reader to the detailed description provided by Huang et al. (2024).

For the FRB fields that contain SDSS data, we follow the strategy outlined in Ata et al. (2021) and extract the ASF in the 10×10 deg^2 region around the position of the FRB from the publicly available MANGLE outputs[19] (Hamilton & Tegmark 2004; Swanson et al. 2008). For the FRB fields containing 6dF survey data, we apply the ASF estimation algorithm in Ata et al. (2021) by comparing the final 6dF DR3 galaxy catalog (Jones et al. 2009) with the map of 6dF on-sky pointings and stellar masks (communicated privately), again over a 10×10 deg^2 field around the FRB. Similarly, the ASF of the AAT survey data is calculated by comparing the number of galaxies with good-quality redshifts to the lists of the selected targets for AAOmega observations combined with the corresponding stellar masks.

Finally, to estimate the RSF in each field, we compute the distribution of observed galaxies in the ARGO reconstruction volumes as a function of comoving distance from the observer in bins of $10\,h^{-1}$ Mpc.

3.5. ARGO Reconstruction Results

Once all the ARGO inputs are prepared, we initialize the reconstructions in each FRB field and run the HMC sampler for 12,000 iterations. We find that the posterior samples have a correlation length of ~100–150, which allows us to extract $N = 61$ posterior realizations of each reconstructed density field, separated by at least 150 iterations on the chain.

In Figures 1 and 2, we show one realization each of the reconstructed matter density field in the foreground of all FRBs in our sample. The density field is smoothed with a Gaussian kernel with the size $R = 0.7\,h^{-1}$ Mpc, and the corresponding redshift space distribution of the galaxies in the "wide-field" sample is shown by the black dots.

Because ARGO yields multiple posterior realizations of the reconstructed matter density field per each FRB foreground region, we are able to not only estimate the integrated DM along the given FRB line of sight but also estimate the corresponding statistical uncertainty of the reconstruction, which we discuss in the next section.

4. DM Model

One of the key characteristics of any FRB signal is the DM—a time delay of the arrival of photons at different frequencies. As an integral measure, it is typical to model the observed $\mathrm{DM_{FRB}}$ as contributions from several components. For each ith FRB in our sample, we assume a model for the observed $\mathrm{DM_{FRB}}$, given by

$$\mathrm{DM_{model},}_i = \mathrm{DM_{MW},}_i + \mathrm{DM_{cosmic},}_i + \mathrm{DM_{host},}_i, \tag{3}$$

[19] https://space.mit.edu/~molly/mangle/download/data.html

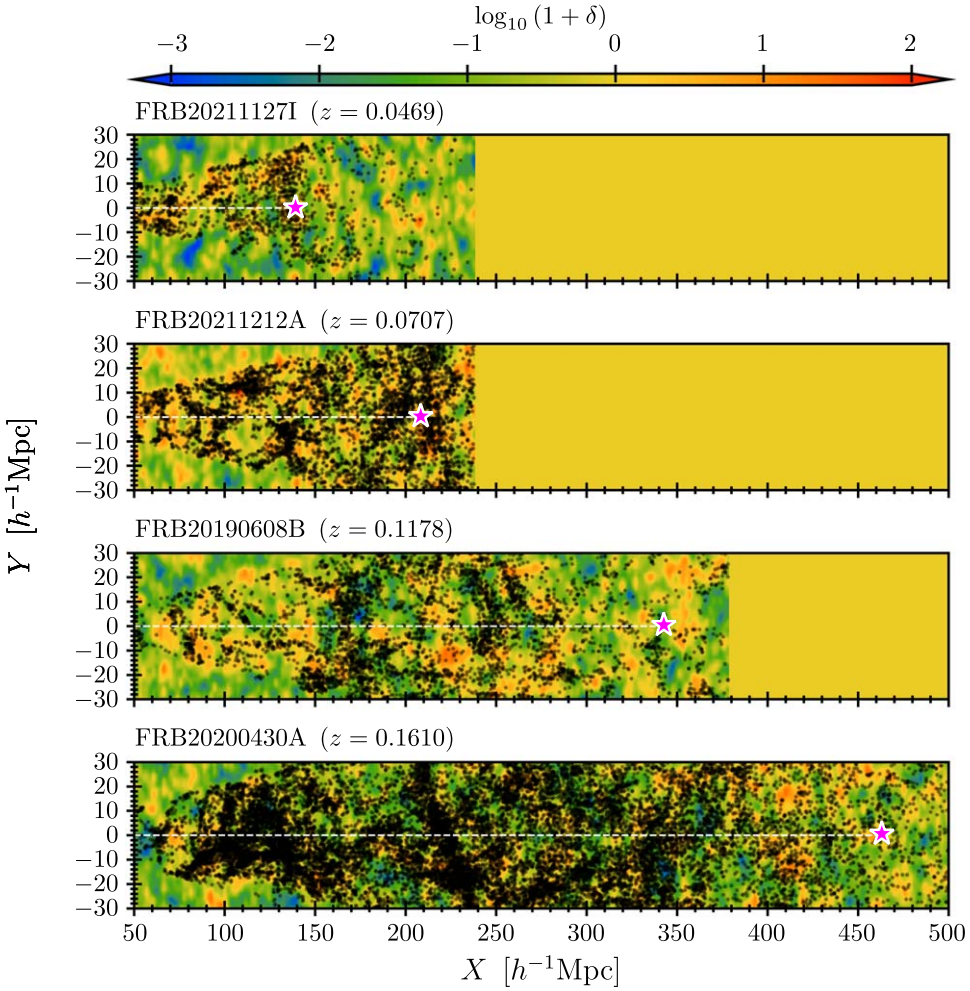

Figure 1. 2D slices through one realization of the matter density fields reconstructed by the ARGO algorithm. The *X*-coordinate increases with cosmic distance, while the *Y*-coordinate is parallel to the sky plane. The *Z*-coordinate is also parallel to the sky plane, but in this projection, we have set it to 0 to center the slices on FRB hosts. The black dots illustrate the spatial distribution of the galaxies in the wide- and narrow-field samples, while the star symbol marks the location of a given FRB host. The dashed line at $Y = 0$ denotes the line of sight of each given FRB.

where $\mathrm{DM_{MW}}$ represents the contribution from the interstellar medium (ISM) and halo of the Milky Way, $\mathrm{DM_{host}}$ comes from the FRB host galaxy, while

$$\mathrm{DM_{cosmic},}_i = \mathrm{DM_{igm,i}} + \mathrm{DM_{halos},}_i \tag{4}$$

is the contribution from the foreground cosmic structures in the diffuse IGM, $\mathrm{DM_{igm}}$, and intersected foreground galactic halos, $\mathrm{DM_{halos}}$, respectively.

Note that in the FRB literature, the notation $\mathrm{DM_{igm}}$ is often used to collectively denote both the IGM and CGM contributions, which we consider separately in Equation (4) and in our analysis. Roughly speaking, $\mathrm{DM_{igm}}$ arises from gas tracing the low-density ($0 \lesssim \rho/\bar{\rho} \lesssim 10$) voids and filaments of the cosmic web, while $\mathrm{DM_{halos}}$ arises from intersections approximately within the virial radii of galactic halos at matter densities of $\rho/\bar{\rho} \gtrsim 10-100$.

In what follows, we discuss these components separately and describe our model and our adopted parameters for DM estimation.

4.1. The Milky Way

The DM contribution from the Milky Way is given by

$$\mathrm{DM_{MW},}_i = \mathrm{DM^{ISM}_{MW},}_i + \mathrm{DM^{halo}_{MW}}, \tag{5}$$

where $\mathrm{DM^{ISM}_{MW},}_i$ arises from the ISM, while $\mathrm{DM^{halo}_{MW}}$ is contributed by the ionized gas in the Milky Way's halo.

In this work, we adopt $\mathrm{DM^{ISM}_{MW}}$ values estimated from the `NE2001` model (Cordes & Lazio 2002) based on their Galactic latitude and longitude, which were conveniently tabulated in James et al. (2022b). The Galactic halo contribution, on the other hand, is given by the estimates of Prochaska & Zheng (2019). In what follows, we adopt the mean value of $\mathrm{DM^{halo}_{MW}} = 40\ \mathrm{pc\ cm^{-3}}$ for each FRB field and include an uncertainty of $\sigma_{\mathrm{MW}} = 15\ \mathrm{pc\ cm^{-3}}$ into the inference algorithm (see Section 5.1). We list the corresponding combined $\mathrm{DM_{MW}}$ values in each FRB field in Table 3.

We note that $\mathrm{DM^{halo}_{MW}}$ remains a highly uncertain quantity. Previous studies place it in the range $10\ \mathrm{pc\ cm^{-3}} \lesssim \mathrm{DM^{halo}_{MW}} \lesssim 111\ \mathrm{pc\ cm^{-3}}$ (Keating & Pen 2020; Cook et al. 2023a; Ravi et al. 2023). However, the exact choice of the mean and the uncertainty on $\mathrm{DM^{halo}_{MW}}$ is a subdominant error component in our analysis given the FLIMFLAM DR1 limited data sample.

4.2. The IGM

The $\mathrm{DM_{igm}}$, arising from the low-density intergalactic gas tracing the large-scale cosmic web along the path *s* to the FRB,

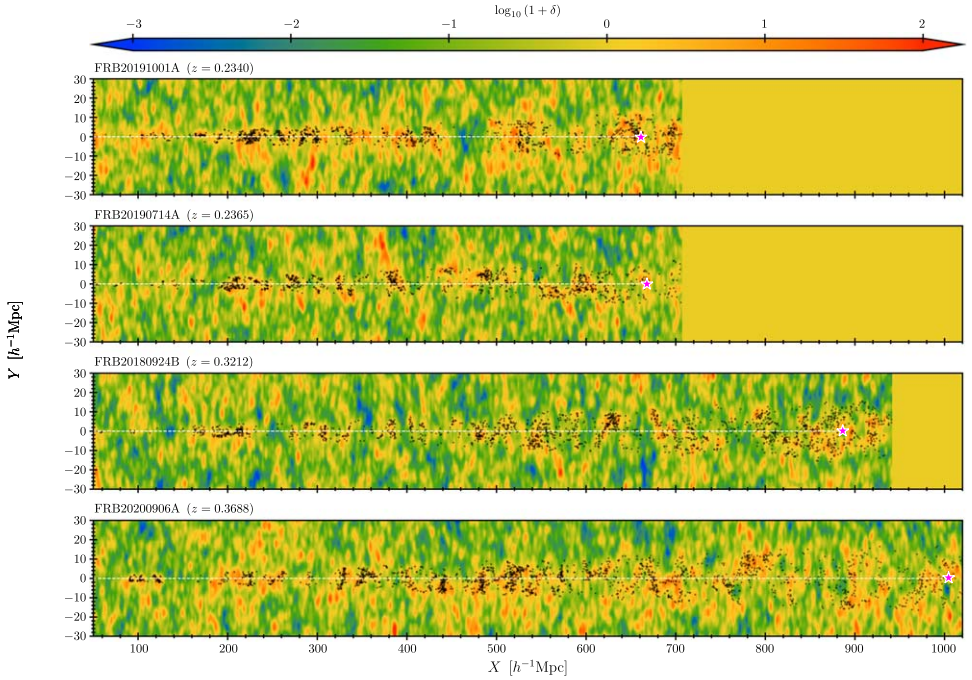

Figure 2. Same as Figure 1 but illustrating the higher-redshift FRBs in our sample.

Table 3
Inferred Values of the DM Components Described in Section 4, Estimated for Each FRB in Our Sample

FRB	Redshift	$\mathrm{DM}_{\mathrm{igm}}^{\mathrm{argo}}$	$\mathrm{DM}_{\mathrm{halos}}$	$\mathrm{DM}_{\mathrm{host}}^{\mathrm{halo}}$	$\langle \log_{10}(M_{\mathrm{host}}^{\mathrm{halo}}/M_{\odot}) \rangle$	$\mathrm{DM}_{\mathrm{MW}}$	$\mathrm{DM}_{\mathrm{FRB}}$
20211127A	0.0469	61.6 ± 32.0	22.6 ± 13.2	24.1 ± 5.5	11.3	82.5	234.83
20211212A	0.0713	171.2 ± 106.4	13.4 ± 15.7	35.8 ± 8.1	11.7	67.1	206.00
20190608A	0.1178	89.9 ± 12.0	30.5 ± 20.4	46.1 ± 10.4	12.1	78.1	339.50
20200430A	0.1608	116.1 ± 5.6	120.0 ± 33.1	24.2 ± 5.7	11.2	67.0	380.10
20191001A	0.2340	466.3 ± 170.4	360.7 ± 72.4	58.1 ± 13.0	12.3	84.7	506.92
20190714A	0.2365	326.5 ± 94.7	321.4 ± 92.1	37.4 ± 8.7	11.8	78.0	504.70
20180924B	0.3212	329.2 ± 91.0	11.5 ± 10.6	44.0 ± 10.4	11.9	81.9	362.40
20200906A	0.3688	559.9 ± 202.8	37.4 ± 23.5	45.8 ± 10.8	11.9	75.9	577.80

Note. From left to right, the columns show the ID of a given FRB, the spectroscopic redshift, the mean and standard deviation of the $\mathrm{DM}_{\mathrm{igm}}$ inferred from the corresponding ARGO reconstructions assuming $f_{\mathrm{igm}} = 1.0$, the mean and standard deviation of the $\mathrm{DM}_{\mathrm{halos}}$ assuming $f_{\mathrm{gas}} = 1.0$ and $r_{\mathrm{max}}/r_{200} = 1.0$, the mean and standard deviation of the FRB host's halo contribution assuming $f_{\mathrm{gas}} = 1.0$, the mean halo mass estimate for each FRB host based on the stellar masses from Gordon et al. (2023), the combined contributions from the Milky Way's ISM and halo components, and the overall observed $\mathrm{DM}_{\mathrm{FRB}}$. All DM values are quoted in units of pc cm^{-3}.

is given by

$$\mathrm{DM}_{\mathrm{igm}} = \int \frac{n_{e,\mathrm{igm}}(s)}{1 + z(s)} ds, \tag{6}$$

where $n_{e,\mathrm{igm}}$ is the number density of free electrons residing in the IGM along the sight line. For each FRB field in our sample, we estimate $\mathrm{DM}_{\mathrm{igm}}$ directly from the ARGO density reconstructions, adopting the discretized version of Equation (6) as follows:

$$\mathrm{DM}_{\mathrm{igm}}^{\mathrm{argo}} = \bar{n}_{e,\mathrm{bar}}(\bar{z}) \sum_{s} (1 + \delta_{m,s}^{\mathrm{sm}}) l_s (1 + z_s)^{-1}, \tag{7}$$

where l_s is the path length to the cell s of the ARGO reconstruction volume along the FRB line of sight, z_s is the corresponding redshift of the cell, and $\delta_{m,s}^{\mathrm{sm}}$ is the smoothed matter overdensity (see example in Figures 1 and 2). The smoothing length is $R = 0.7\,h^{-1}$ Mpc, which was found by Lee et al. (2022) to allow dark-matter-only N-body simulations with $1.875\,h^{-1}$ Mpc grid cells to match the global $\mathrm{DM}_{\mathrm{igm}}$ distribution in cosmological hydrodynamical simulations. We define $\bar{n}_{e,\mathrm{bar}}(\bar{z})$ as the mean cosmic density of electrons at the median redshift $\bar{z}$ traversed by the ensemble of FRB paths, defined as

$$\bar{n}_{e,\mathrm{bar}}(\bar{z}) = \Omega_b \bar{\rho}_c(\bar{z}) \left[\frac{m_{\mathrm{He}}(1 - Y) + 2 Y m_{\mathrm{H}}}{m_{\mathrm{He}} m_{\mathrm{H}}} \right], \tag{8}$$

where m_{H} and m_{He} are the atomic masses of hydrogen and helium atoms, respectively; $Y_{\mathrm{He}} = 0.243$ is the cosmic mass fraction of doubly ionized helium; $\Omega_b = 0.044$ is the cosmic baryon density; and $\bar{\rho}_c(\bar{z})$ is the critical density of the Universe. As written, $\bar{n}_{e,\mathrm{bar}}$ assumes that all baryons in the Universe are ionized and reside in the IGM. We can further introduce f_{igm}, the fraction of all cosmic baryons residing in the IGM, which will be one of the free parameters in our analysis. Thus,

$$\bar{n}_{e,\mathrm{igm}} \equiv f_{\mathrm{igm}}\ \bar{n}_{e,\mathrm{bar}} \tag{9}$$

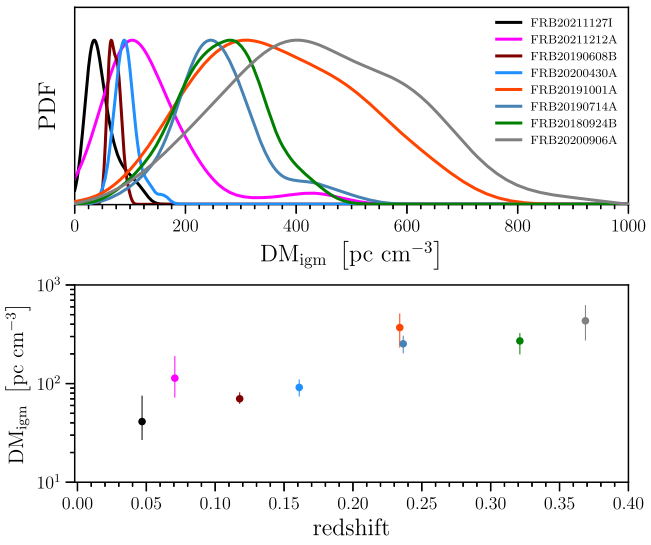

Figure 3. Top: KDE-smoothed probability density function (PDF) of the $\mathrm{DM_{igm}}$ distributions estimated for each considered FRB field from the corresponding ARGO reconstructions, with $f_{\rm igm} = 0.8$ for illustrative purposes. Bottom: estimated values of $\mathrm{DM_{igm}}$ from ARGO reconstructions as a function of FRB redshift. Each marker is the 50th percentile of the corresponding distribution from the top panel, while the error bars are given by 16th and 84th percentiles of the same distributions.

is the actual mean number density of free electrons in the IGM as constrained by our data. To tie together Equations (6), (7), (8), and (9) with the current limited data set, we will constrain $f_{\rm igm}$ as a free parameter assuming a fixed redshift of $\bar{z} \simeq 0.20$, which is approximately the median redshift probed by the DR1 FRB sight lines.

The top panel of Figure 3 shows inferred distributions of $\mathrm{DM_{igm}}$ in each FRB field in our sample, evaluated from the corresponding $N_{\rm real} = 61$ posterior realizations of the matter density field estimated by ARGO. As discussed in Section 3.1, to take into account the first $50\,h^{-1}$ Mpc, excluded from ARGO reconstructions, we add $15\,\mathrm{pc\,cm^{-3}}$ to each individual $\mathrm{DM_{igm}}$ posterior value. From each $\mathrm{DM_{igm}}$ distribution, we then calculate the mean, $\langle \mathrm{DM_{igm}^{argo}} \rangle$, and standard deviation, $\sigma_{\rm igm}^{\rm argo}$, and plot the results as a function of FRB redshift in the bottom panel of Figure 3.

We adopt the median of the ARGO realizations for each FRB, scaled by $f_{\rm igm}$, as the IGM contribution to our model DM in Equation (3), given by

$$\mathrm{DM_{igm},}_i = f_{\rm igm} \sum_j^{N_{\rm real}} \frac{\mathrm{DM_{igm,}}_{ij}^{\rm argo}}{N_{\rm real}}, \tag{10}$$

for each FRB sight line i.

4.3. The Intervening Halos

To model the contribution of the foreground halos to the observed DM, in each FRB field, we adopt the modified Navarro–Frank–White model (mNFW; Prochaska & Zheng 2019) to estimate the radial density distribution of the gas in each galaxy halo from the corresponding "narrow-field" sample (see Section 2.2). In this model, the baryon density is given by

$$\rho_b(r) = f_{\rm gas} \frac{\Omega_b}{\Omega_m} \frac{\rho_0(M_{\rm halo})}{y^{1-\alpha}(y_0 + y)^{2+\alpha}}, \tag{11}$$

where $f_{\rm gas}$ is the fraction of cosmic baryons residing in the CGM of each individual galactic halo relative to the total amount of baryons within the halo if the cosmic baryon fraction were assumed, i.e., $M_{\rm cgm} = f_{\rm gas}\,(\Omega_b/\Omega_m) M_{\rm halo}$; ρ_0 is the central density of the halo as a function of halo mass $M_{\rm halo}$; $y \equiv c(r/r_{200})$, where c is the concentration parameter; and y_0 and α are the mNFW profile parameters. In this work, we use the fiducial values $y_0 = \alpha = 2$ from Prochaska & Zheng (2019) and adopt $f_{\rm gas}$ as another free model parameter in our model DM.

As described in Section 3.2, we use CIGALE to estimate the stellar masses of the galaxies in the "narrow-field" samples. We then convert the average stellar masses found by CIGALE to the corresponding halo masses, $M_{\rm halo}$, by adopting the mean stellar-to-halo mass relation described in Moster et al. (2013).

Similar to the discussion in Section 3.3, we use the FoF finder to check if any of the galaxies in the "narrow-field" sample are members of groups and/or clusters. If any groups are found, we remove the entries of the member galaxies from our list and add the information on their respective groups. Figure 4 illustrates all foreground halos of galaxies and groups found in the foreground of all FRB sight lines. The circles illustrate the corresponding sizes of the halo's virial radii (only to scale in the vertical direction, transverse to the line of sight), while the colors indicate the average halo masses inferred from CIGALE.

The overall distribution of halo masses, intersected by the FRB sight lines, is shown in Figure 5. We mostly probe halos with masses of $10^{11}\,M_\odot \lesssim M_{\rm halo} \lesssim 10^{12.5}\,M_\odot$, although a small number of our halos are approaching the dwarf galaxy regime ($M_{\rm halo} \sim 10^{10}$–$10^{11}\,M_\odot$), while at the other extreme, we probe several galaxy group halos with $M_{\rm halo} \sim 10^{13}\,M_\odot$.

Note that in contrast to Lee et al. (2022), who assumed the mNFW truncation radius $r_{\rm max}$ as a free parameter, we adopt a fixed $r_{\rm max} = r_{200}$. While the exact size of the galactic halos is not well constrained, Simha et al. (2020) showed that extending the mNFW profiles to $2 \times r_{200}$ can double the $\mathrm{DM_{halos}}$ contribution (see also Prochaska & Zheng 2019; Lee et al. 2023). These results suggest that, in principle, the extent of galactic halos should be included as another free parameter (similar to the discussion in Lee et al. 2022). However, the present DR1 sample is of limited constraining power, and the truncated mNFW profile is in any case an approximation. In this work, we therefore adopt a fixed truncation radius and leave more refined parameterization to future work with larger samples.

Finally, to obtain the cumulative $\mathrm{DM_{halos,}}_i$ along the line of sight of the ith FRB, we sum up the DMs of all individual foreground halos that are found by integrating their respective mNFW profiles in Equation (11). The integration is performed along the intersecting paths of the FRB sight line corresponding to the impact parameters $b_\perp$ of the foreground halos, determined by their respective redshifts and angular positions.

So far, we have considered only the average halo masses of the foreground halos. However, there are considerable uncertainties in the stellar mass estimation from the SED fitting technique. These uncertainties, as well as the scatter in the stellar mass–halo mass relationship, propagate into the $\mathrm{DM_{halos,}}_i$ calculation. In order to take them into account, we introduce a relative random scatter, $\sigma_{M_{\rm halo}}(\log_{10}[M_{\rm halo}/M_\odot]) = 0.3$ dex, to the inferred halo masses. This is the typical uncertainty in converting M_* to $M_{\rm halo}$ for $M_* = 10^{10.5}\ M_\odot$ galaxies

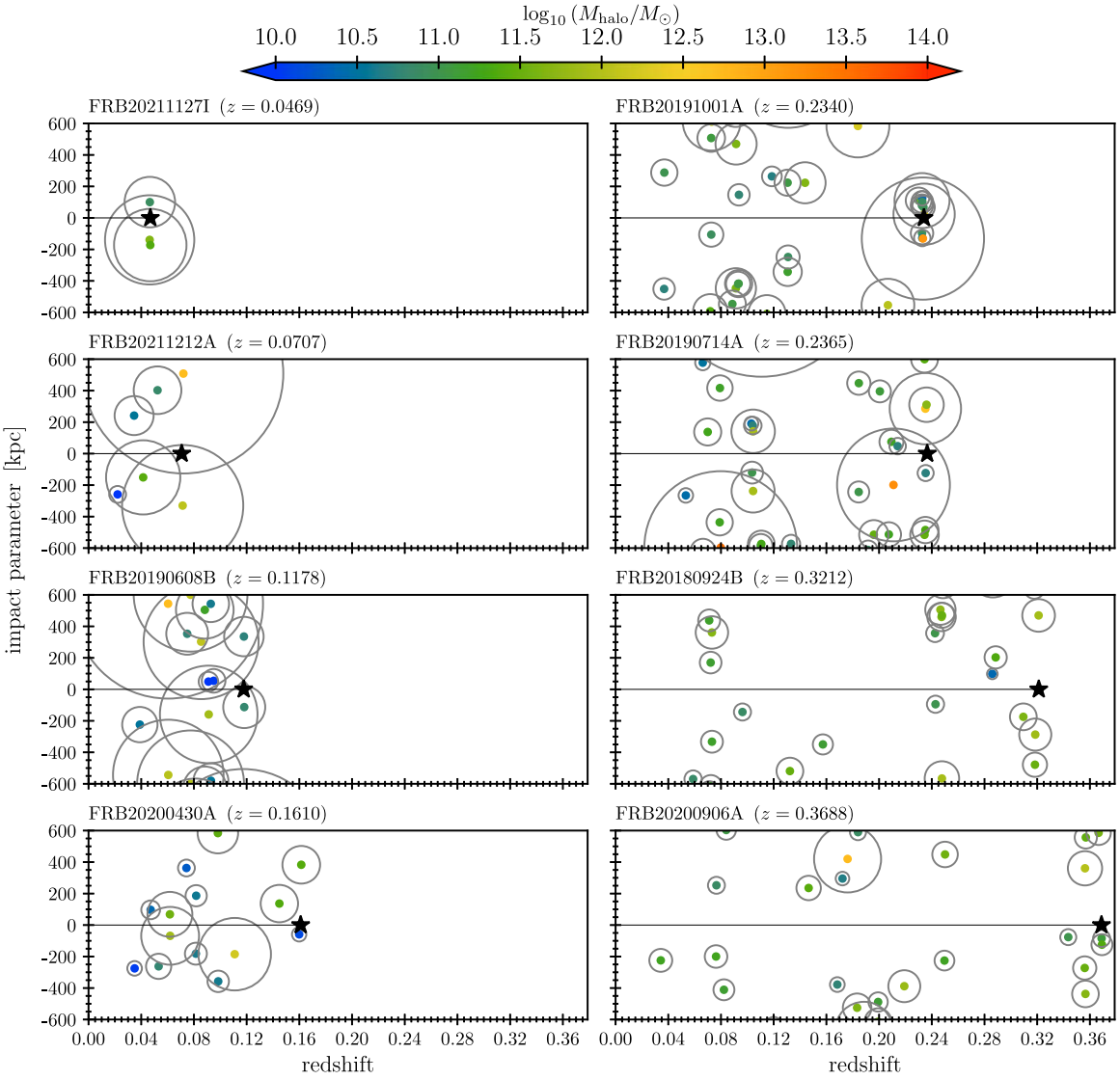

Figure 4. Observed distribution of foreground halos of galaxies and groups around the line of sight of the FRBs in the sample. The circles show the estimated size of the halos, r_{200}, given the mean estimate of the corresponding halo masses. The sizes of the halos are only valid along the y-axis; for visualization purposes, the circles representing halo sizes are not to scale along the x-axis. The color of the points represents the halo masses as given by the color bar.

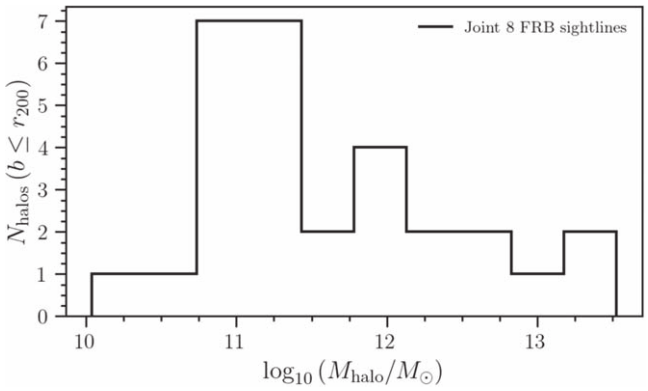

Figure 5. Distribution of the intersected foreground halo masses in the FLIMFLAM DR1 sample. Only halos with impact parameters smaller than the corresponding r_{200} radius (assuming the mean halo mass estimate from CIGALE) of our FRB sight lines are plotted.

(Simha et al. 2021). For each "narrow-field" galaxy catalog of each FRB sight line, we generate $N_{\rm real} = 1000$ Monte Carlo realizations of the $\mathrm{DM}_{\mathrm{halos},i}$, where we randomly sample combinations of halo masses that would be consistent with the mean and scatter of the intervening galaxies' halo masses. For a given FRB sight line i, we compute the mean of these $N_{\rm real} = 1000$ realizations, scaled by $f_{\rm gas}$, and incorporate it in our model of the observed DM as

$$\mathrm{DM}_{\mathrm{halos},i} = f_{\rm gas}\,\frac{1}{N_{\rm real}}\sum_{j}^{N_{\rm real}}\sum_{k}^{N_{\rm halos}}\frac{\mathrm{DM}^{j}_{\mathrm{halo},k}}{1+z_{\mathrm{halo},k}}, \tag{12}$$

where the $\mathrm{DM}_{\mathrm{halo},k}$ of each k foreground halo is corrected for the redshift dilation by a factor of $1/(1+z_{\mathrm{halo},k})$. On the other hand, the standard deviation $\sigma_{\mathrm{halos},i}$ of the resulting Monte Carlo realizations of $\mathrm{DM}_{\mathrm{halos},i}$ is then adopted for the likelihood calculation for the MCMC analysis (see Section 5.1).

We illustrate the resulting distribution of $\mathrm{DM}_{\mathrm{halos},i}$ along each FRB sight line in the top panel of Figure 6. For illustrative purposes, we adopt a value of $f_{\rm gas} = 0.25$. The bottom panel of Figure 6, meanwhile, shows the mean and standard deviation of these distributions as a function of the free parameter $f_{\rm gas}$.

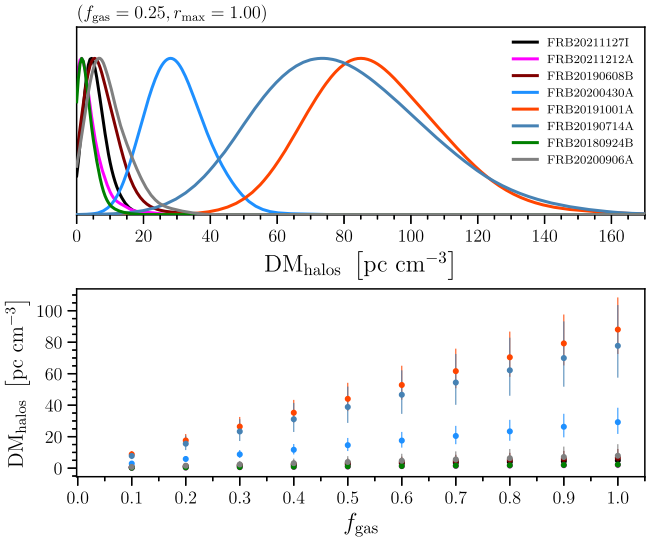

Figure 6. Top: KDE-smoothed PDF of the $\rm DM_{halos}$ distributions estimated for each considered FRB field. Bottom: estimated values of $\rm DM_{halos}$ as a function of $f_{\rm gas}$. Each marker is the 50th percentile of the corresponding distribution from the top panel, while the error bars are given by 16th and 84th percentiles of the same distributions.

4.4. The Hosts

The contribution to the observed DM from the FRB host galaxies remains a highly uncertain quantity. Previous studies have often either used a constant value or estimated it from an assumed probability density distribution (e.g., Macquart et al. 2020; James et al. 2022a, 2022b; but see L. Bernales-Cortes et al. 2024, in preparation, for an empirical estimation). In this work, we employ the following model for the $\rm DM_{host}$:

$$\rm DM_{host,\it i} = \frac{DM^{halo}_{host,\it i} + \langle DM^{unk}_{host}\rangle}{1 + z_{frb,\it i}}, \tag{13}$$

where $\rm DM^{halo}_{host,\it i}$ is the contribution from the CGM halo of the FRB host galaxy and $\langle \rm DM^{unk}_{host}\rangle$ is left as a free parameter in our inference model, describing the unknown contributions from the host ISM, the FRB engine, and its immediate surroundings.

In order to estimate $\rm DM^{halo}_{host,\it i}$ for a given FRB, we follow Section 4.3 and use the mNFW model to calculate the halo density profile of the host galaxy, given published estimates of its stellar mass (Gordon et al. 2023). To obtain the $\rm DM^{halo}_{host,\it i}$, we then integrate the resulting density profile along the path determined by the FRB impact parameter relative to the center of the host galaxy. In contrast to $\rm DM_{halos}$, here we integrate only half of the halo. Similar to the discussion in Section 4.3, we take into account the uncertainty in the measured masses of the host galaxies' halos by introducing a random scatter $\sigma(\log_{10}[M^{\rm halo}_{\rm host}/M_\odot]) = 0.30$ dex. For each FRB host, we then compute the mean and standard deviation, $\sigma^{\rm halo}_{{\rm host},i}$, of $N_{\rm real} = 1000$ Monte Carlo realizations of the $\rm DM^{halo}_{host}$ given by

$$\rm DM^{halo}_{host,\it i} = \it f_{\rm gas}\, \frac{1}{N_{real}} \sum_{j}^{N_{real}} DM^{halo}_{host}(\it M^{halo}_{host,\it j}). \tag{14}$$

We note that the FRB 20191001A host galaxy is a special case among the DR1 sample because it has been found to reside within a galaxy group based on the methodology described in Section 3.3 (see also Bhandari et al. 2020). As discussed in Section 4.3, we replace the information about the individual members with the corresponding properties of the group itself (mass, impact parameter, etc.) and use them to estimate the contribution that we assign to the $\rm DM_{halos}$ ($\rm DM = 166 \pm 50\,pc\,cm^{-3}$). On the other hand, to calculate the $\rm DM^{halo}_{host}$, we adopt the mean stellar/halo mass of the host galaxy itself and find $\rm DM^{halo}_{host} = 58.1 \pm 13.0\,pc\,cm^{-3}$ (assuming $f_{\rm gas} = 1.0$) in the case of FRB 20191001A (see Table 3). In other words, we include the contribution from both the host galaxy and its galaxy group, albeit in different DM terms. This assumption should be tested with cosmological hydrodynamical simulations in future work.

FRB 20191001A is, to our knowledge, the fourth FRB known to reside within a galaxy group or cluster (Connor et al. 2023; Gordon et al. 2023), and it will be interesting to follow up such objects in future analyses to investigate the possible insights this might have on the FRB host population.

5. Parameter Inference

In this section, we describe our inference algorithm and the corresponding model parameters governing the evolution of DM components, discussed in Section 4. We begin with the definition of the likelihood function, required by the MCMC algorithm later.

5.1. The Likelihood

We assume that the joint likelihood function $\mathcal{L}_{\rm frb}(\rm DM_{frb}|\Theta)$ for eight FRBs in our sample (see Table 1) is well described by a Gaussian,

$$\ln \mathcal{L}(\rm DM_{FRB}|\Theta) \propto -\frac{1}{2}\sum_{i}^{N_{frb}}\left[\frac{(\rm DM_{model,\it i}(\Theta) - DM_{FRB,\it i})^2}{\sigma_i^2}\right], \tag{15}$$

where $\Theta = \{f_{\rm igm}, f_{\rm gas}, \langle \rm DM^{unk}_{host}\rangle\}$ represents our model parameters; $\rm DM_{model,\it i}$ is the model DM, described in detail in the previous section; and the model variance σ_i^2 is estimated by combining in quadrature uncertainties on the individual components of the total $\rm DM_{model,\it i}$, given by

$$\begin{aligned}\sigma_i^2 = (\sigma^{\rm argo}_{{\rm igm},i})^2 + (\sigma_{{\rm halos},i})^2 + (\sigma^{\rm unk}_{\rm host})^2 \\ + (\sigma^{\rm halo}_{{\rm host},i})^2 + (\sigma_{{\rm MW},i})^2,\end{aligned} \tag{16}$$

where we omit the uncertainty on the observed $\rm DM_{FRB}$ because it is negligible in comparison to other considered uncertainties. For a given value of $\langle \rm DM^{unk}_{host}\rangle$, we assume a lognormal distribution such that the corresponding variance $(\sigma^{\rm unk}_{\rm host})^2$ is described by

$$(\sigma^{\rm unk}_{\rm host})^2 = (e^{\sigma_*^2} - 1)e^{(2\mu+\sigma_*^2)}, \tag{17}$$

where $\mu \equiv \langle \rm DM^{unk}_{host}\rangle$, and we use the best-fit value $\sigma_* = 1.23$ from James et al. (2022a).[20]

5.2. The Priors

For the FLIMFLAM DR1 analysis, we will adopt several combinations of physically motivated priors that we will describe here, summarized in Table 4. In all cases, we assume a

[20] James et al. (2022a) reported the standard deviation of the lognormal $\rm DM_{host}$ distribution in $\log_{10}$ units ($\sigma = 0.53$). We rescaled it by a factor of $1/\log_{10} e$ in order to convert to the natural logarithm units.

Table 4
Bayesian Prior Combinations

	Flat $f_{\rm d}$ (Fiducial)	Flat $f_{\rm d}$ + Limited $f_{\rm gas}$	Gaussian $f_{\rm d}$	Gaussian $f_{\rm d}$ + Limited $f_{\rm gas}$
$\pi(f_{\rm igm})$	(0, 1.00]	(0, 1.00]	(0, 1.00]	(0, 1.00]
$\pi(f_{\rm gas})$	(0, 1.00]	(0, 0.70]	(0, 1.00]	(0, 0.70]
$\pi(\ln {\rm DM}_{\rm host}^{\rm unk})$	[0, 6.00]	[0, 6.00]	[0, 6.00]	[0, 6.00]
$\pi(f_{\rm d})$	[0.75, 0.95]	[0.75, 0.95]	$\mathcal{N}(\mu = 0.86, \sigma = 0.02)$	$\mathcal{N}(\mu = 0.86, \sigma = 0.02)$

flat linear prior on the fraction of cosmic baryons inside the IGM, i.e., $\pi(f_{\rm igm}) = (0.0, 1.0]$. Similarly, also in all cases, we adopt a flat logarithmic prior on the unknown FRB host contribution $\pi(\ln\langle {\rm DM}_{\rm host}^{\rm unk}\rangle) = [0.0, 6.0]$, consistent with the ranges explored by James et al. (2022b).

For $f_{\rm gas}$, we take as the default case a flat prior spanning all physical values between 0 and unity: $\pi(f_{\rm gas}) = (0.0, 1.0]$. However, recently, Khrykin et al. (2023) explored the evolution of the cosmic baryon fractions in and around simulated halos in the Simba suite of cosmological hydrodynamical simulations (Davé et al. 2019). They found that the $f_{\rm gas}$ value depends significantly on both the considered halo mass range and the exact feedback prescription used in the simulations. For the range of halo masses estimated for the foreground galaxies/groups in the FLIMFLAM DR1 sample used in this work (see Figure 5), the results of Khrykin et al. (2023) suggest a range of $f_{\rm gas} = (0, 0.70]$ for all feedback prescriptions they considered. We therefore also consider an additional "limited $f_{\rm gas}$" prior with $\pi(f_{\rm gas}) = (0.0, 0.7]$.

We also include additional priors describing the total budget of baryons expected to be found in the diffuse states outside of individual galaxies,

$$\begin{aligned} f_{\rm d} &\equiv f_{\rm igm} + f_{\rm cgm} + f_{\rm icm} \\ &= 1 - f_{*} - f_{\rm bh} - f_{\rm ism}, \end{aligned} \tag{18}$$

where $f_{\rm icm}$ is the fraction of all cosmic baryons that reside within the intracluster media (ICM) of galaxy clusters with $M_{\rm halo} \gtrsim 10^{14}\, M_{\odot}$ and $f_{\rm cgm}$ is the fraction in lower-mass halos. Our free parameters are related to Equation (18) through $f_{\rm igm}$ explicitly and $f_{\rm cgm}$, which is a function of $f_{\rm gas}$. Meanwhile, $f_{\rm icm}$ is constrained by ICM gas mass fraction ($f_{\rm gas,icm}$) measurements using X-ray (e.g., Gonzalez et al. 2013; Chiu et al. 2018) and Sunyaev–Zel'dovich (e.g., de Graaff et al. 2019) observations.

The overall $f_{\rm d}(z)$ can be estimated by the process of elimination: one estimates the total observed budget of stars, f_{*}; stellar remnants (neutron stars and black holes), $f_{\rm bh}$; and ISM in galaxies, $f_{\rm ism}$, and then subtracts these from the total cosmic baryon to yield $f_{\rm d}$ as seen in the second line of Equation (18). To calculate $f_{\rm d}(z)$, we follow the calculation presented in Macquart et al. (2020) and encoded in the FRB repository.[21] The error in $f_{\rm d}(z)$ is dominated by the systematic uncertainty in the stellar mass density ρ_{*}, which depends on an assumed stellar IMF. The values reported by Madau & Dickinson (2014), which are the defaults, assume the Salpeter IMF (Salpeter 1955). If we instead adopt the Chabrier IMF (Chabrier 2003), the ρ_{*} values decrease by 1.7 and $f_{\rm d}(z)$ increases at $z = 0$ from $\approx$0.84 to $\approx$0.9. The resulting $f_{\rm d}(z)$ is shown as a function of redshift in Figure 7. We use the $f_{\rm d}$ evaluated at $\bar{z} = 0.20$, the mean redshift probed by our sight lines, and implement it as a prior in two ways: (i) as a flat prior such that $f_{\rm d}(z) = [0.75, 0.95]$ ("flat $f_{\rm d}$") or (ii) as a Gaussian prior with a mean of $\mu = 0.86$ and standard deviation $\sigma = 0.02$ ("Gaussian $f_{\rm d}$").

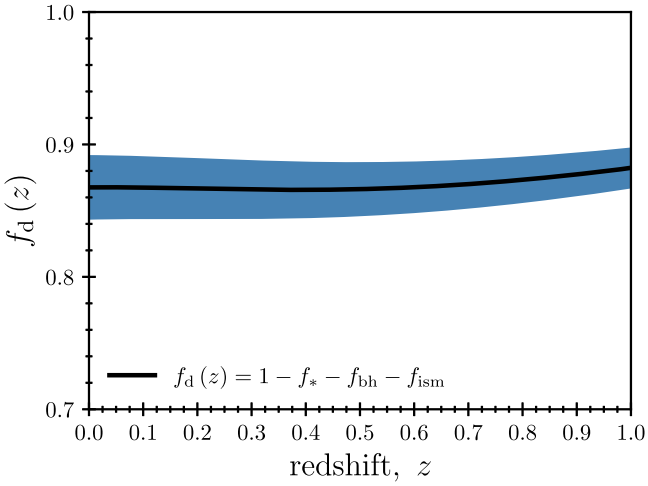

Figure 7. Evolution of the cosmic diffuse baryon fraction $f_{\rm d}$ as a function of redshift. The shaded area illustrates the 2σ error bars.

Our analysis aims to constrain as one of our free parameters the quantity $f_{\rm gas}$, which represents the fraction of baryons residing in the CGM on a per-halo basis. Therefore, in order to use the prior in Equation (18), we need to convert $f_{\rm gas}$ to $f_{\rm cgm}$, which is the fraction of cosmic baryons residing in all the halos in the Universe. For a range of the halo masses $[M_1, M_2]$, $f_{\rm cgm}$ is given by

$$\begin{aligned} f_{\rm cgm} &= \frac{1}{(\Omega_b/V)\int_V \bar{\rho}_{\rm m}(z)dV} \\ &\times \int_{M_1}^{M_2}\left[\int_0^{r_{\rm max}} f_{\rm gas}\,\Omega_b \rho_{\rm halo}(M_{\rm halo}, z, r) 4\pi r^2 dr\right] \\ &\times \phi(M_{\rm halo})\, d\ln\frac{M_{\rm halo}}{M_{\odot}}, \end{aligned} \tag{19}$$

where $\bar{\rho}_{\rm m}(z)$ is the cosmic matter density at a given redshift, $\rho_{\rm halo}(z, r)$, the radial matter density profile of collapsed halos with mass $M_{\rm halo}$, and $\phi(M_{\rm halo})$ is the halo mass function (see more the detailed discussion in Khrykin et al. 2023). The conversion between $f_{\rm gas,icm}$ and $f_{\rm icm}$ is similar, except that the mass range is specifically set to $M_{\rm halo} \geqslant 10^{14}\, M_{\odot}$. In the case of the ICM, we assume a fixed $f_{\rm gas,icm} = 0.8$ with a Gaussian standard deviation of $\sigma = 0.1$, which is consistent with current measurements of gas in galaxy clusters (Gonzalez et al. 2013; Chiu et al. 2018). Adopting the halo mass function from the

[21] https://github.com/FRBs/FRB

Aemulus package (McClintock et al. 2019) and assuming the mean redshift of our sample $\bar{z} \simeq 0.20$ and $r_{\rm max} = 1.0 \times r_{200}$, we precompute a lookup reference table between $f_{\rm gas}$ and $f_{\rm cgm}$ values (and, equivalently, $f_{\rm gas,icm}$ and $f_{\rm icm}$) using Equation (19).

While the definition of $f_{\rm cgm}$ in Equation (18) is supposed to span the entire range of noncluster halo masses in the Universe ($M < 10^{14}\,M_{\odot}$), the FLIMFLAM DR1 "narrow-field" foreground data do not fully cover this entire mass range (Figure 5). We therefore further split $f_{\rm cgm}$ into two terms, $f_{\rm cgm} = f_{\rm cgm,ff} + f_{\rm cgm,other}$. The $f_{\rm cgm,ff}$ represents the halo mass range sampled by our data, for which $f_{\rm gas}$ is a free parameter. For halo masses not represented by our data, $f_{\rm cgm,other}$ is the unknown contribution to the cosmic budget. We assume that the $f_{\rm gas}$ for these halos can span $0 < f_{\rm gas} \leqslant 1$ with uniform probability.

Consequently, at each MCMC step, the proposed value of $f_{\rm gas}$ is then converted to $f_{\rm cgm,ff}$, while random realizations of $f_{\rm icm}$ and $f_{\rm cgm,other}$ are drawn, making the aforementioned assumptions for their respective $f_{\rm gas}$. These terms are then compared to $f_{\rm d}$ in Equation (18) to apply the aforementioned prior.

Note that, in general, $f_{\rm gas}$ is expected to be a function of halo mass (Ayromlou et al. 2023; Khrykin et al. 2023). Future analyses should adopt more sophisticated parameterization, but for FLIMFLAM DR1, the simplified assumption described above should suffice given the limited data.

6. Results

Given the expression for the joint likelihood in Equation (15) and the choice of priors described in Section 5.2, we now proceed to sample the aforementioned likelihood function using the MCMC algorithm in order to estimate the posterior probability distributions for the model parameters $f_{\rm igm}$, $f_{\rm gas}$, and $\langle {\rm DM}^{\rm unk}_{\rm host} \rangle$. We adopt the publicly available affine-invariant MCMC sampling algorithm `EMCEE` (Foreman-Mackey et al. 2013).

The results of the MCMC inference are shown in Figure 8, where the 2D contours illustrate the 95% (gray) and 68% (black) confidence intervals, respectively. 1D marginalized posterior probability distributions for each model parameter are also shown by the corresponding histograms, while the values are tabulated in Table 5.

For the purpose of the discussion, we adopt the flat-$f_{\rm d}$-only case as the fiducial prior (see Table 4). In this case, we estimate the IGM baryon fraction to be $f_{\rm igm} = 0.59^{+0.11}_{-0.10}$ and the unknown DM contribution from the host ISM and FRB engine to be $\langle {\rm DM}^{\rm unk}_{\rm host} \rangle = 69^{+28}_{-19}$ pc cm^{-3}.

On the other hand, the results presented in Figure 8 indicate that the current sample of FRBs used in this work has only limited sensitivity to the $f_{\rm gas}$ value: we find $f_{\rm gas} = 0.55^{+0.26}_{-0.29}$, and within the 95th confidence level, the 1D and 2D contours span the entire range of allowed $f_{\rm gas}$ values (Figure 8). Applying Equation (19), this implies that $f_{\rm cgm,ff} = 0.20^{+0.10}_{-0.11}$ of the baryons in the Universe exist as CGM gas surrounding halos with $10^{11}\,M_{\odot} \lesssim M_{\rm halo} \lesssim 10^{13}\,M_{\odot}$. There is a degeneracy between $f_{\rm igm}$ and $f_{\rm gas}$ primarily set by the prior constraints on the total number of diffuse baryons, $f_{\rm d}$, residing outside of galaxies (see Section 5.2).

In comparison with the fiducial flat $f_{\rm d}$ prior, changing to the Gaussian $f_{\rm d}$ case leads to negligible changes to the resulting parameter constraints and errors at the $\sim$1% level. However, adopting a more limited range of $f_{\rm gas} = (0.00,\ 0.70]$ as suggested by hydrodynamical simulations (Khrykin et al. 2023) leads to more noticeable differences. As expected, $f_{\rm gas}$ is reduced from $f_{\rm gas} = 0.55^{+0.26}_{-0.29}$ in the fiducial case to $f_{\rm gas} = 0.44^{+0.18}_{-0.24}$, corresponding to a CGM fraction of $f_{\rm cgm,ff} = 0.16^{+0.07}_{-0.09}$ for our halo mass range. With the reduction of $f_{\rm gas}$ from the limited $f_{\rm gas}$ prior, $f_{\rm igm}$ also increases along the $f_{\rm igm}$–$f_{\rm gas}$ degeneracy direction to $f_{\rm igm} = 0.63^{+0.09}_{-0.07}$. The difference in the recovered 1D marginalized posterior distributions of each parameter in different MCMC runs is shown in Figure 9.

Our constraints of $f_{\rm igm} \approx 0.59$–0.64 are consistent with an IGM that has experienced no galaxy feedback of any kind, which should yield $f_{\rm igm} \approx 0.59$ according to the cosmological hydrodynamical simulations analyzed by Khrykin et al. (2023). However, irrespective of the chosen priors, given the uncertainties, our resulting constraints on $f_{\rm igm}$ are also consistent with an IGM that has experienced stellar feedback ($f_{\rm igm} \simeq 0.70$ per Khrykin et al. 2023). On the other hand, Khrykin et al. (2023) showed that AGN jet feedback ejects significant numbers of baryons out into the IGM, resulting in higher IGM baryon fractions in the relevant simulations: $f_{\rm igm} \approx 0.85$–0.87. Therefore, our constraints mildly disfavor the AGN jet feedback scenario at the 2σ level.

For all the prior combinations we have considered here, however, the resulting constraints on the "unknown" host ISM and host engine contribution to ${\rm DM}_{\rm host}$ remain consistently at $\langle {\rm DM}^{\rm unk}_{\rm host} \rangle \approx 70$ pc cm^{-3}. This indicates that our data are successful at separating out the ${\rm DM}_{\rm host}$ component from the total observed DM, even though we only weakly constrain the further separation of the ${\rm DM}_{\rm igm}$ and ${\rm DM}_{\rm halos}$ components.

As mentioned in Section 4.4, the contribution of the FRB host galaxy ${\rm DM}_{\rm host}$ to the observed DM is driven by two components: the host's extended CGM halo ${\rm DM}^{\rm halo}_{\rm host}$ and the hitherto unconstrained input from the host's stellar/ISM environment and the FRB progenitor itself or its immediate surroundings, $\langle {\rm DM}^{\rm unk}_{\rm host} \rangle$. Following Equation (13), we can estimate the mean total host contribution $\langle {\rm DM}_{\rm host} \rangle$, averaged over our eight FRB sight lines, which is given by

$$\langle {\rm DM}_{\rm host} \rangle = \frac{1}{N_{\rm frb}} \sum_{i}^{N_{\rm frb}} f_{\rm gas}\, {\rm DM}^{\rm halo}_{{\rm host},i} + \langle {\rm DM}^{\rm unk}_{\rm host} \rangle, \tag{20}$$

where we omitted the factor of $1/(1 + z_{\rm frb})$ in Equation (20) since it was already taken into account previously (see discussion in Sections 4.4).

To fully capture the covariance between $f_{\rm gas}$ and $\langle {\rm DM}^{\rm unk}_{\rm host} \rangle$ estimated by the MCMC algorithm in Section 5, we sample the posterior pairs of these parameters from the corresponding MCMC chains. Moreover, for each pair of $f_{\rm gas}$ and $\langle {\rm DM}^{\rm unk}_{\rm host} \rangle$ drawn from the MCMC chain, we additionally randomly choose a value of the host galaxy halo mass from the corresponding Gaussian distribution (see Section 4.4) and calculate the ${\rm DM}^{\rm halo}_{{\rm host},i}$ in Equation (20). This results in $\approx$10,000 realizations of $\langle {\rm DM}_{\rm host} \rangle$ per each MCMC run. Finally, we estimate the corresponding 16th, 50th, and 84th percentiles of these distributions. We report the resulting average host galaxy contribution to the observed DM and the corresponding uncertainties in the last row of Table 5.

In all considered prior combinations, we find consistent mean values of $\langle {\rm DM}_{\rm host} \rangle \approx 86$–$90$ pc cm^{-3} and comparable uncertainties. This value is somewhat lower than that reported by James et al. (2022a; and subsequently Baptista et al. 2023). In their analysis of nearly 70 FRBs, they found

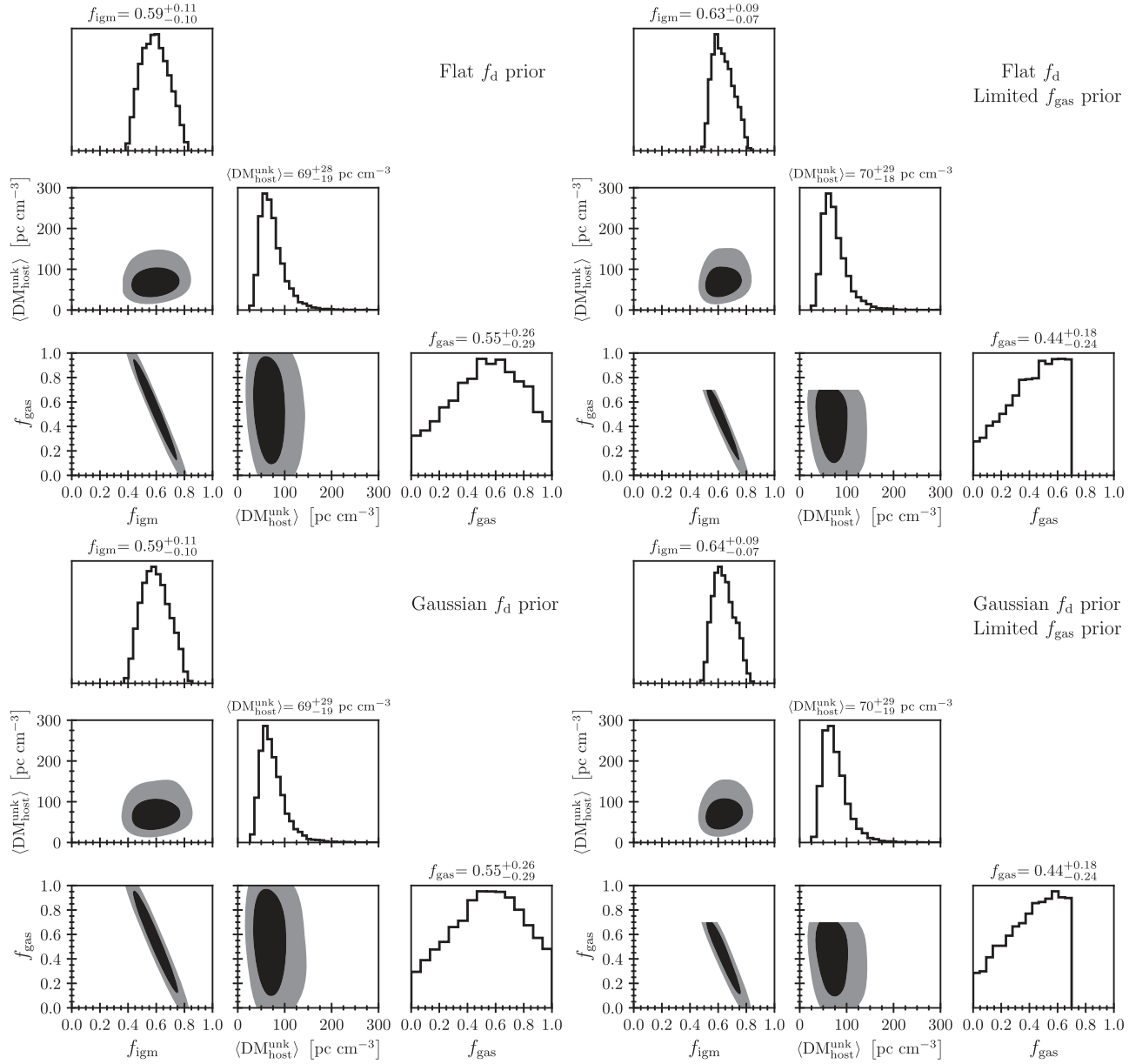

Figure 8. Results of the MCMC inference on the observed sample of FRBs in Table 1. The panels show inferred 2D contours and marginalized 1D posterior probabilities of the model parameters. The black and gray contours correspond to the 68% and 95% confidence regions, respectively. Each triangle plot corresponds to a specific choice of priors. See text for details.

Table 5
Results of the MCMC Analysis for Different Sets of Priors $\pi(\Theta)$

	Flat $f_{\rm d}$ (Fiducial)	Flat $f_{\rm d}$ + Limited $f_{\rm gas}$	Gaussian $f_{\rm d}$	Gaussian $f_{\rm d}$ + Limited $f_{\rm gas}$
$f_{\rm igm}$	$0.59^{+0.11}_{-0.10}$	$0.63^{+0.09}_{-0.07}$	$0.59^{+0.11}_{-0.10}$	$0.64^{+0.09}_{-0.07}$
$f_{\rm gas}$	$0.55^{+0.26}_{-0.29}$	$0.44^{+0.18}_{-0.24}$	$0.55^{+0.26}_{-0.29}$	$0.44^{+0.18}_{-0.24}$
$\langle {\rm DM}^{\rm unk}_{\rm host} \rangle$	69^{+28}_{-19} pc cm^{-3}	70^{+29}_{-18} pc cm^{-3}	69^{+29}_{-19} pc cm^{-3}	70^{+29}_{-19} pc cm^{-3}
$\langle {\rm DM}_{\rm host} \rangle$	90^{+29}_{-19} pc cm^{-3}	86^{+28}_{-18} pc cm^{-3}	90^{+31}_{-20} pc cm^{-3}	87^{+29}_{-19} pc cm^{-3}

Note. The last row shows the values of the total host contribution (both from the corresponding halo and the unknown contribution from the host's ISM and FRB engine) averaged over eight FRB sight lines used in this work.

$\langle {\rm DM}_{\rm host} \rangle \approx 130^{+66}_{-48}$ pc cm^{-3} and a lognormal scatter of $\log_{10}\sigma \simeq 0.50$.

Although our $\langle {\rm DM}_{\rm host} \rangle$ is formally consistent with their result, we believe our lower value can probably be explained by the fact that we have explicitly rejected from our sample FRBs believed to have large $\langle {\rm DM}_{\rm host} \rangle$, e.g., FRB 20210117A (Simha et al. 2023) and FRB 20190520B (Lee et al. 2023). James et al. (2022a), on the other hand, did not make use of any foreground

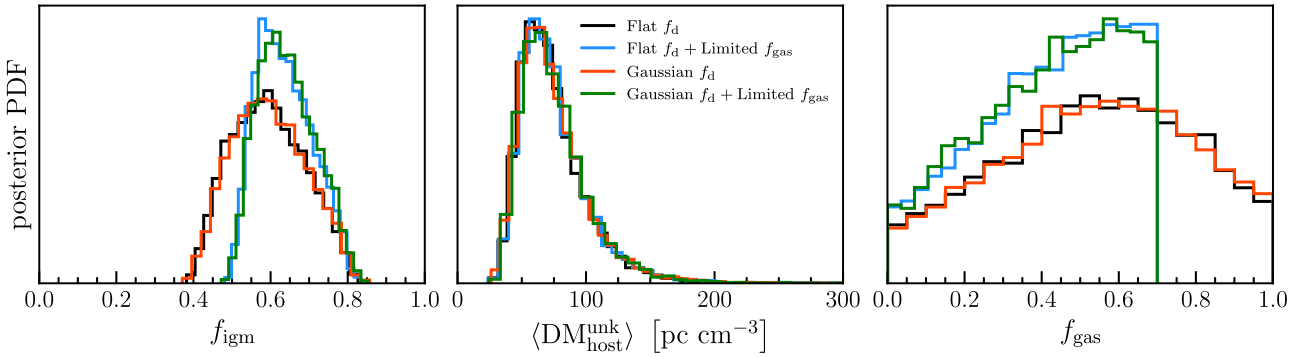

Figure 9. 1D marginalized posterior distributions for each model parameter, estimated using different combinations of the priors. The black curve shows the results corresponding to the fiducial set of priors, discussed in Section 5.2, whereas the other curves correspond to the modified priors on $f_{\rm gas}$ and $f_{\rm d}(z)$.

information, and therefore such excess-DM objects would have been included. In the future, it is possible that other measured FRB quantities, such as the scattering time (e.g., Cordes et al. 2022) or Hα emission measure (Tendulkar et al. 2017), could be used as priors for the $\rm DM^{unk}_{host}$ contribution from individual FRBs in the analysis sample (L. Bernales-Cortes et al. 2024, in preparation).

7. Conclusions

In this work, we presented the analysis of the first data release of the FLIMFLAM survey, aimed at revealing the distribution of the comic baryons within the diffuse IGM as well as the CGM gas of galaxy halos.

We have conducted an extensive observational campaign to collect wide-field spectroscopic information on galaxies in the foreground of eight localized FRBs at $z \lesssim 0.4$ (with a mean redshift of $\bar{z} \simeq 0.20$ probed by the sample). This information has been used in the state-of-the-art ARGO Bayesian statistical algorithm to reconstruct the matter density field along each FRB sight line, permitting models for the contribution of the diffuse IGM gas to the observed FRB DMs. We have also collected narrow-field spectroscopic data about the foreground halos intersected by the FRB. This allowed us to estimate their contribution to the observed FRB $\rm DM_{FRB}$.

We have then utilized a Bayesian algorithm to statistically compare the observed FRB DMs to the theoretical model predictions. The main results of our work are as follows.

1. Assuming the fiducial set of flat priors on the model parameters, we measure the fraction of baryons residing in the IGM to be $f_{\rm igm} = 0.59^{+0.11}_{-0.10}$ and the corresponding $f_{\rm cgm} = 0.20^{+0.10}_{-0.11}$ of baryons in the Universe inside the CGM of $10^{10}\ M_\odot \lesssim M_{\rm halo} \lesssim 10^{13}\ M_\odot$ halos. Imposing a more strict prior on $f_{\rm gas}$, motivated by the hydrodynamical simulations, modifies this partition of cosmic baryons to $f_{\rm igm} = 0.63^{+0.09}_{-0.07}$ and $f_{\rm cgm} = 0.16^{+0.07}_{-0.09}$, respectively.
2. Our results on $f_{\rm igm}$ so far appear to be consistent with the predictions of recent hydrodynamical simulations for the IGM gas. However, given the large uncertainties in this preliminary sample, we cannot rule out any of the feedback models analyzed by Khrykin et al. (2023).
3. Based on our sample, we find that the host galaxies on average contribute $\langle \rm DM_{host} \rangle = 90^{+29}_{-19}$ pc cm^{-3} to the observed $\rm DM_{FRB}$ (fiducial priors), while the major part of it is coming from the "unknown" host ISM and/or FRB engine, adding on average $\langle \rm DM^{unk}_{host} \rangle = 69^{+28}_{-19}$ pc cm^{-3}. This is the first analysis to attempt to separate out these components.

The information, encoded in the foreground structures traversed by the FRB, is paramount for placing high-precision constraints on cosmological and astrophysical parameters (e.g., Simha et al. 2020, 2023; Lee et al. 2023). The future complete FLIMFLAM sample of $N \simeq 20$ FRBs will provide a more robust estimate of both, the distribution of baryons and the involvement of various feedback mechanisms in shaping it. Beyond FLIMFLAM, increasing localization efforts by CRAFT (Macquart et al. 2010), the MeerKAT TRAnsients and Pulsars (Sanidas et al. 2018), and the Deep Synoptic Array (Kocz et al. 2019), coupled with observational campaigns on 4 m class multiplexed instruments such as DESI (Levi et al. 2013), will achieve detailed measurements of the cosmic baryon distribution in the low-redshift Universe ($z \lesssim 0.3$) on samples of $N \gtrsim 100$ FRBs.

Acknowledgments

We thank Elmo Tempel for kindly providing his group-finding software. Kavli IPMU is supported by World Premier International Research Center Initiative (WPI), MEXT, Japan. This work was performed in part at the Center for Data-Driven Discovery, Kavli IPMU (WPI). I.S.K. and N.T. would like to acknowledge the support received by the Joint Committee ESO-Government of Chile grant ORP 40/2022. R.M.S. acknowledges support through the Australian Research Council Future Fellowship FT190100155. R.M.S. and A.T.D. acknowledge support through the Australian Research Council Discovery Project DP220102305. J.X.P., S.S., A.C.G., and the Fong Group at Northwestern acknowledge support by the National Science Foundation under grant Nos. AST-1909358 and AST-2308182 and CAREER grant No. AST-2047919. A.C.G. acknowledges support from NSF grants AST-1911140, AST-1910471, and AST-2206490 as a member of the Fast and Fortunate for FRB Follow-up team. L.M. acknowledges the receipt of an MQ-RES scholarship from Macquarie University. M.G. is supported by the Australian Government through the Australian Research Council's Discovery Projects funding scheme (DP210102103).

Parts of this research were supported by the Australian Research Council Centre of Excellence for All Sky Astrophysics in 3 Dimensions (ASTRO 3D) through project No. CE170100013. Based in part on data acquired at the Anglo-Australian Telescope under programs A/2020B/04, O/2021A/3001, A/2021A/13, A/2021B/9, and A/2022A/9. We acknowledge the traditional

custodians of the land on which the AAT stands, the Gamilaraay people, and pay our respects to elders past and present.

The data presented herein were obtained at the W. M. Keck Observatory (PIDs: U051, U100, and U162), which is operated as a scientific partnership among the California Institute of Technology, the University of California, and the National Aeronautics and Space Administration. The Observatory was made possible by the generous financial support of the W. M. Keck Foundation. We also wish to recognize and acknowledge the very significant cultural role and reverence that the summit of Maunakea has always had within the indigenous Hawaiian community. We are most fortunate to have the opportunity to conduct observations from this mountain.

Based on observations collected at the European Southern Observatory under ESO programs 2102.A-5005(A), 0104.A-0411(A), 105.20HG.001, 110.241Y.001, and 110.241Y.002.

Based on observations obtained at the international Gemini Observatory (PID: GS-2022B-Q-137), a program of NSF NOIRLab, which is managed by the Association of Universities for Research in Astronomy (AURA) under a cooperative agreement with the U.S. National Science Foundation on behalf of the Gemini Observatory partnership: the U.S. National Science Foundation (United States), National Research Council (Canada), Agencia Nacional de Investigación y Desarrollo (Chile), Ministerio de Ciencia, Tecnología e Innovación (Argentina), Ministério da Ciência, Tecnologia, Inovações e Comunicações (Brazil), and Korea Astronomy and Space Science Institute (Republic of Korea).

This scientific work uses data obtained from Inyarrimanha Ilgari Bundara/the Murchison Radio-astronomy Observatory. We acknowledge the Wajarri Yamaji people as the traditional owners and native titleholders of the observatory site. CSIRO's ASKAP radio telescope is part of the Australia Telescope National Facility (https://ror.org/05qajvd42). Operation of ASKAP is funded by the Australian Government with support from the National Collaborative Research Infrastructure Strategy. ASKAP uses the resources of the Pawsey Supercomputing Research Centre. Establishment of ASKAP, Inyarrimanha Ilgari Bundara, the CSIRO Murchison Radio-astronomy Observatory, and the Pawsey Supercomputing Research Centre are initiatives of the Australian Government, with support from the Government of Western Australia and the Science and Industry Endowment Fund.

This research has made use of data obtained from the SuperCOSMOS Science Archive, prepared and hosted by the Wide Field Astronomy Unit, Institute for Astronomy, University of Edinburgh, which is funded by the UK Science and Technology Facilities Council.

This publication makes use of data products from the Two Micron All Sky Survey, which is a joint project of the University of Massachusetts and the Infrared Processing and Analysis Center/California Institute of Technology, funded by the National Aeronautics and Space Administration and the National Science Foundation.

This research has made use of the NASA/IPAC Extragalactic Database (NED), which is operated by the Jet Propulsion Laboratory, California Institute of Technology, under contract with the National Aeronautics and Space Administration. This publication makes use of data products from the Wide-field Infrared Survey Explorer, which is a joint project of the University of California, Los Angeles, and the Jet Propulsion Laboratory/California Institute of Technology, funded by the National Aeronautics and Space Administration.

Facilities: AAT (2dF-AAOmega), VLT (MUSE), Keck (DEIMOS, LRIS, KCWI).

Software: MARZ (Hinton et al. 2016), Astropy (Astropy Collaboration et al. 2022), Numpy (Harris et al. 2020), EMCEE (Foreman-Mackey et al. 2013), CIGALE (Baptista et al. 2023), Matplotlib (Hunter 2007).

ORCID iDs

Ilya S. Khrykin https://orcid.org/0000-0003-0574-7421
Metin Ata https://orcid.org/0000-0002-5934-9018
Khee-Gan Lee https://orcid.org/0000-0001-9299-5719
Sunil Simha https://orcid.org/0000-0003-3801-1496
Yuxin Huang https://orcid.org/0000-0002-0298-8898
J. Xavier Prochaska https://orcid.org/0000-0002-7738-6875
Nicolas Tejos https://orcid.org/0000-0002-1883-4252
Keith W. Bannister https://orcid.org/0000-0003-2149-0363
Jeff Cooke https://orcid.org/0000-0001-5703-2108
Cherie K. Day https://orcid.org/0000-0002-8101-3027
Adam Deller https://orcid.org/0000-0001-9434-3837
Marcin Glowacki https://orcid.org/0000-0002-5067-8894
Alexa C. Gordon https://orcid.org/0000-0002-5025-4645
Clancy W. James https://orcid.org/0000-0002-6437-6176
Lachlan Marnoch https://orcid.org/0000-0003-1483-0147
Ryan. M. Shannon https://orcid.org/0000-0002-7285-6348
Jielai Zhang https://orcid.org/0000-0001-5310-4186
Lucas Bernales-Cortes https://orcid.org/0009-0002-9608-9275

References

Abazajian, K. N., Adelman-McCarthy, J. K., Agüeros, M. A., et al. 2009, ApJS, 182, 543
Abbott, T. M. C., Adamów, M., Aguena, M., et al. 2021, ApJS, 255, 20
Aggarwal, K., Budavári, T., Deller, A. T., et al. 2021, ApJ, 911, 95
Astropy Collaboration, Price-Whelan, A. M., Lim, P. L., et al. 2022, ApJ, 935, 167
Ata, M., Kitaura, F.-S., Lee, K.-G., et al. 2021, MNRAS, 500, 3194
Ata, M., Kitaura, F.-S., & Müller, V. 2015, MNRAS, 446, 4250
Ata, M., Kitaura, F.-S., Chuang, C.-H., et al. 2017, MNRAS, 467, 3993
Ayromlou, M., Nelson, D., & Pillepich, A. 2023, MNRAS, 524, 5391
Bannister, K. W., Deller, A. T., Phillips, C., et al. 2019, Sci, 365, 565
Baptista, J., Prochaska, J. X., Mannings, A. G., et al. 2024, ApJ, 965, 57
Bhandari, S., Sadler, E. M., Prochaska, J. X., et al. 2020, ApJL, 895, L37
Blanton, M. R., Schlegel, D. J., Strauss, M. A., et al. 2005, AJ, 129, 2562
Boquien, M., Burgarella, D., Roehlly, Y., et al. 2019, A&A, 622, A103
Bruzual, G., & Charlot, S. 2003, MNRAS, 344, 1000
Calzetti, D. 2001, PASP, 113, 1449
Cen, R., & Ostriker, J. P. 1999, ApJ, 514, 1
Chabrier, G. 2003, PASP, 115, 763
Chambers, K. C., Magnier, E. A., Metcalfe, N., et al. 2016, arXiv:1612.05560
Chiu, I., Mohr, J. J., McDonald, M., et al. 2018, MNRAS, 478, 3072
Connor, L., Ravi, V., Catha, M., et al. 2023, ApJL, 949, L26
Cook, A. M., Bhardwaj, M., Gaensler, B. M., et al. 2023a, ApJ, 946, 58
Cook, D. O., Mazzarella, J. M., Helou, G., et al. 2023b, ApJS, 268, 14
Cooke, R. J., Pettini, M., & Steidel, C. C. 2018, ApJ, 855, 102
Cordes, J. M., & Lazio, T. J. W. 2002, arXiv:astro-ph/0207156
Cordes, J. M., Ocker, S. K., & Chatterjee, S. 2022, ApJ, 931, 88
Dale, D. A., Helou, G., Magdis, G. E., et al. 2014, ApJ, 784, 83
Davé, R., Anglés-Alcázar, D., Narayanan, D., et al. 2019, MNRAS, 486, 2827
de Graaff, A., Cai, Y.-C., Heymans, C., & Peacock, J. A. 2019, A&A, 624, A48
Dey, A., Schlegel, D. J., Lang, D., et al. 2019, AJ, 157, 168
Duane, S., Kennedy, A. D., Pendleton, B. J., & Roweth, D. 1987, PhLB, 195, 216
Foreman-Mackey, D., Hogg, D. W., Lang, D., & Goodman, J. 2013, PASP, 125, 306
Fukugita, M., Hogan, C. J., & Peebles, P. J. E. 1998, ApJ, 503, 518

Gonzalez, A. H., Sivanandam, S., Zabludoff, A. I., & Zaritsky, D. 2013, ApJ, 778, 14
Gordon, A. C., Fong, W.-f., Kilpatrick, C. D., et al. 2023, ApJ, 954, 80
Gunn, J. E., & Peterson, B. A. 1965, ApJ, 142, 1633
Hamilton, A. J. S., & Tegmark, M. 2004, MNRAS, 349, 115
Harris, C. R., Millman, K. J., van der Walt, S. J., et al. 2020, Natur, 585, 357
Heintz, K. E., Prochaska, J. X., Simha, S., et al. 2020, ApJ, 903, 152
Hinton, S. R., Davis, T. M., Lidman, C., Glazebrook, K., & Lewis, G. F. 2016, A&C, 15, 61
Hunter, J. D. 2007, CSE, 9, 90
Huang, Y., Simha, S., Khrykin, I., et al. 2024, arXiv:2408.12864
James, C. W., Prochaska, J. X., Macquart, J. P., et al. 2022a, MNRAS, 509, 4775
James, C. W., Ghosh, E. M., Prochaska, J. X., et al. 2022b, MNRAS, 516, 4862
Jasche, J., & Kitaura, F. S. 2010, MNRAS, 407, 29
Jones, D. H., Read, M. A., Saunders, W., et al. 2009, MNRAS, 399, 683
Keating, L. C., & Pen, U.-L. 2020, MNRAS, 496, L106
Khrykin, I. S., Sorini, D., Lee, K.-G., & Davé, R. 2024, MNRAS, 529, 537
Kitaura, F. S., & Enßlin, T. A. 2008, MNRAS, 389, 497
Kitaura, F.-S., Jasche, J., & Metcalf, R. B. 2010, MNRAS, 403, 589
Kocz, J., Ravi, V., Catha, M., et al. 2019, MNRAS, 489, 919
Lee, K.-G., Ata, M., Khrykin, I. S., et al. 2022, ApJ, 928, 9
Lee, K.-G., Khrykin, I. S., Simha, S., et al. 2023, ApJL, 954, L7
Lehner, N., Savage, B. D., Richter, P., et al. 2007, ApJ, 658, 680
Levi, M., Bebek, C., Beers, T., et al. 2013, arXiv:1308.0847
Lorimer, D. R., Bailes, M., McLaughlin, M. A., Narkevic, D. J., & Crawford, F. 2007, Sci, 318, 777
Macquart, J.-P., Bailes, M., Bhat, N. D. R., et al. 2010, PASA, 27, 272
Macquart, J. P., Prochaska, J. X., McQuinn, M., et al. 2020, Natur, 581, 391
Madau, P., & Dickinson, M. 2014, ARA&A, 52, 415
McClintock, T., Rozo, E., Becker, M. R., et al. 2019, ApJ, 872, 53
Moster, B. P., Naab, T., & White, S. D. M. 2013, MNRAS, 428, 3121
Narayanan, A., Wakker, B. P., & Savage, B. D. 2009, ApJ, 703, 74
Neal, R. 2011, Handbook of Markov Chain Monte Carlo (London: Chapman & Hall), 113
Nevalainen, J., Tempel, E., Liivamägi, L. J., et al. 2015, A&A, 583, A142
Nicastro, F., Kaastra, J., Krongold, Y., et al. 2018, Natur, 558, 406
Petroff, E., Hessels, J. W. T., & Lorimer, D. R. 2022, A&ARv, 30, 2
Planck Collaboration, Aghanim, N., Akrami, Y., et al. 2020, A&A, 641, A6
Prochaska, J. X., Weiner, B., Chen, H. W., Mulchaey, J., & Cooksey, K. 2011, ApJ, 740, 91
Prochaska, J. X., & Zheng, Y. 2019, MNRAS, 485, 648
Ravi, V., Catha, M., Chen, G., et al. 2023, arXiv:2301.01000
Salpeter, E. E. 1955, ApJ, 121, 161
Sanidas, S., Caleb, M., Driessen, L., et al. 2018, in IAU Symp. 337, Pulsar Astrophysics the Next Fifty Years, ed. P. Weltevrede et al. (Cambridge: Cambridge Univ. Press), 406
Schlegel, D. J., Finkbeiner, D. P., & Davis, M. 1998, ApJ, 500, 525
Simha, S., Burchett, J. N., Prochaska, J. X., et al. 2020, ApJ, 901, 134
Simha, S., Tejos, N., Prochaska, J. X., et al. 2021, ApJ, 921, 134
Simha, S., Lee, K.-G., Prochaska, J. X., et al. 2023, ApJ, 954, 71
Skrutskie, M. F., Cutri, R. M., Stiening, R., et al. 2006, AJ, 131, 1163
Sorini, D., Davé, R., Cui, W., & Appleby, S. 2022, MNRAS, 516, 883
Swanson, M. E. C., Tegmark, M., Hamilton, A. J. S., & Hill, J. C. 2008, MNRAS, 387, 1391
Tago, E., Einasto, J., Saar, E., et al. 2008, A&A, 479, 927
Tejos, N., Prochaska, J. X., Crighton, N. H. M., et al. 2016, MNRAS, 455, 2662
Tempel, E., Tago, E., & Liivamägi, L. J. 2012, A&A, 540, A106
Tempel, E., Tamm, A., Gramann, M., et al. 2014, A&A, 566, A1
Tendulkar, S. P., Bassa, C. G., Cordes, J. M., et al. 2017, ApJL, 834, L7
Tripp, T. M., Sembach, K. R., Bowen, D. V., et al. 2008, ApJS, 177, 39